

Using rotation measure grids to detect cosmological magnetic fields – a Bayesian approach

V. Vacca¹, N. Oppermann², T. Enßlin^{1,3}, J. Jasche^{4,5}, M. Selig^{1,3,6}, M. Greiner^{1,3}, H. Junklewitz⁷, M. Reinecke¹, M. Brüggen⁸, E. Carretti⁹, L. Feretti¹⁰, C. Ferrari¹¹, C. A. Hales^{12,13}, C. Horellou¹⁴, S. Ideguchi¹⁵, M. Johnston-Hollitt¹⁶, R. F. Pizzo¹⁷, H. Röttgering¹⁸, T. W. Shimwell¹⁸, and K. Takahashi¹⁹

¹ Max Planck Institute for Astrophysics, Karl-Schwarzschild-Str. 1, 85748 Garching, Germany

² Canadian Institute for Theoretical Astrophysics, University of Toronto, 60 St. George Street, Toronto ON, M5S 3H8, Canada

³ Ludwig-Maximilians - Universität München, Geschwister-Scholl-Platz 1, 80539, München, Germany

⁴ CNRS, UMR 7095, Institut d'Astrophysique de Paris, 98 bis, boulevard Arago, F-75014 Paris, France

⁵ Excellence Cluster Universe, Boltzmannstr. 2, D-85748 Garching, Germany

⁶ IBM Deutschland Research and Development GmbH Schönaicher Straße 220, D-71032 Böblingen

⁷ Argelander-Institut für Astronomie, Auf dem Hügel 71, 52121 Bonn, Germany

⁸ Hamburger Sternwarte, University of Hamburg, Gojenbergsweg 112, D-21029 Hamburg, Germany

⁹ INAF-Osservatorio Astronomico di Cagliari, Via della Scienza 5, 09047 Selargius (CA), Italy

¹⁰ INAF-Istituto di Radioastronomia, via Gobetti 101, 40129 Bologna, Italy

¹¹ Laboratoire Lagrange, Université Côte d'Azur, Observatoire de la Côte d'Azur, CNRS, Blvd de l'Observatoire, CS 34229, 06304 Nice cedex 4, France

¹² National Radio Astronomy Observatory, PO Box 0, Socorro, NM 87801, USA

¹³ Jansky Fellow of the National Radio Astronomy Observatory

¹⁴ Department of Earth and Space Sciences, Chalmers University of Technology, OSO, SE-439 92 Onsala, Sweden

¹⁵ Department of Physics, UNIST, Ulsan 689-798, Korea

¹⁶ School of Chemical & Physical Sciences, Victoria University of Wellington, PO Box 600, Wellington 6014, New Zealand

¹⁷ ASTRON, Postbus 2, 7990 AA, Dwingeloo, The Netherlands

¹⁸ Leiden Observatory, Leiden University, PO Box 9513, NL-2300 RA, Leiden, the Netherlands

¹⁹ Kumamoto University, 2-39-1, Kurokami, Kumamoto 860-8555, Japan

Received MM DD, YY; accepted MM DD, YY

ABSTRACT

Determining magnetic field properties in different environments of the cosmic large-scale structure as well as their evolution over redshift is a fundamental step toward uncovering the origin of cosmic magnetic fields. Radio observations permit the study of extragalactic magnetic fields via measurements of the Faraday depth of extragalactic radio sources. Our aim is to investigate how much different extragalactic environments contribute to the Faraday depth variance of these sources. We develop a Bayesian algorithm to distinguish statistically Faraday depth variance contributions intrinsic to the source from those due to the medium between the source and the observer. In our algorithm the Galactic foreground and the measurement noise are taken into account as the uncertainty correlations of the galactic model. Additionally, our algorithm allows for the investigation of possible redshift evolution of the extragalactic contribution. This work presents the derivation of the algorithm and tests performed on mock observations. With cosmic magnetism being one of the key science projects of the new generation of radio interferometers we have made predictions for the algorithm's performance on data from the next generation of radio interferometers. Applications to real data are left for future work.

Key words. Methods: data analysis – methods: statistical – magnetic fields – polarization – large-scale structure of Universe

1. Introduction

The origin and evolution of cosmic magnetism are at present poorly understood. Answering the many open questions surrounding the physics of astrophysical magnetic fields is a difficult task since magnetic fields can be significantly affected by structure and galaxy formation and evolution processes. Their strength can be amplified for example in galaxy clusters by mergers, and in galaxies by large-scale dynamos, invoking differential rotation and turbulence. Insights into the origin and properties of magnetic fields in the Universe could be provided by probing them on even larger scales. Along filaments and voids of the cosmic web, turbulent intracluster gas motions have not yet enhanced the magnetic field; its strength thus still depends

on the seed field intensity, in contrast to galaxy clusters, where it probably mostly reflects the present level of turbulence (see e.g., Donnert et al. 2009; Xu et al. 2010, 2011). Intervening magneto-ionic media cause a difference in the phase velocity between the left-handed and right-handed circular polarization components of the linearly polarized synchrotron radiation emitted by a background radio source (e.g. Carilli & Taylor 2002; Govoni & Feretti 2004). This effect translates into a rotation of the intrinsic polarization angle, ψ_0 ,

$$\psi(\lambda^2) = \psi_0 + \phi\lambda^2. \quad (1)$$

Following Burn (1966), the observed polarization angle, ψ , depends on the observation wavelength, λ , through the Faraday

depth, ϕ ,

$$\phi = a_0 \int_0^{z_s} B_l(z) n_e(z) \frac{dl}{dz} dz, \quad (2)$$

where a_0 depends only on fundamental constants, n_e is the electron density, B_l the component of the magnetic field along the line of sight, and z_s the redshift of the source. When the rotation is completely due to a foreground screen, the Faraday depth has the same value as the rotation measure (RM), defined by

$$\text{RM} \equiv \frac{\partial \psi}{\partial \lambda^2}. \quad (3)$$

The Faraday depth is assumed to be positive when the line of sight average component of the magnetic field points toward the observer, otherwise it is negative for a field with an average component pointing away from the observer. The amount of Faraday depth measured by radio observations along a given line of sight is the sum of the contributions from the Milky Way, the emitting radio source and any other sources and large-scale structures in between hosting a magnetized plasma. The investigation of these contribution and of their possible dependence on redshift is essential in order to discriminate among the different scenarios of magnetic field formation and evolution and therefore crucial for the understanding of cosmic magnetism. Sensitive observations, a good knowledge of the Galactic Faraday foreground screen, and a statistical approach able to properly combine all the observational information are necessary. An all-sky map of the Galactic Faraday rotation foreground and an estimate of the overall extragalactic contribution has been derived by Oppermann et al. (2012, 2015) in the framework of *Information Field Theory* (Enßlin et al. 2009), by assuming a correlated Galactic foreground and a completely uncorrelated extragalactic term. In this paper, we propose a new, fully Bayesian, approach aiming at further disentangling the contribution intrinsic to emitting sources from the contribution due to the intergalactic environment between the source and the observer, and at investigating the dependence of these contributions on redshift.

The first direct proof of the existence of magnetic fields in large-scale extragalactic environments, i.e., galaxy clusters, dates back to the 1970s with the discovery of extended, diffuse, central synchrotron sources called radio halos (see e.g. Feretti et al. 2012 for a review). Later, indirect evidence of the existence of intracluster magnetic fields has been given by several statistical studies on the effect of the Faraday rotation on the radio signal from background galaxies or galaxies embedded in galaxy clusters (Lawler & Dennison 1982; Vallée et al. 1986; Clarke et al. 2001; Johnston-Hollitt 2003; Clarke 2004; Johnston-Hollitt & Ekers 2004). On scales up to a few Mpc from the nearest galaxy cluster, possibly along filaments, only a few diffuse synchrotron sources have been reported (Harris et al. 1993; Bagchi et al. 2002; Kronberg et al. 2007; Giovannini et al. 2013, 2015). Magnetic fields with strengths of the order of 10^{-15} G in voids might be indicated by γ -ray observations (see Neronov & Vovk 2010; Tavecchio et al. 2010; Takahashi et al. 2012, 2013, but see Broderick et al. 2014a,b for alternative possibilities). Nevertheless, up to now, a robust confirmed detection of magnetic fields on scales much larger than clusters is not available. Stasyszyn et al. (2010) and Akahori et al. (2014a) investigated the possibility to statistically measure Faraday rotation from intergalactic magnetic fields with present observations, showing that only the Square Kilometre Array (SKA) and its pathfinders are likely to succeed in this respect. By comparing the observations with single-scale magnetic field simulations, Pshirkov et al. (2015)

infer an upper limit of 1.2 nG for extragalactic large-scale magnetic fields, while the Planck Collaboration (2015) derived a more stringent upper limit for primordial large-scale magnetic fields of $B < 0.67$ nG from the analysis of the CMB power spectra and the effect on the ionization history (but see also Takahashi et al. 2005; Ichiki et al. 2006).

A number of authors examined a possible dependence of extragalactic Faraday depths on the redshift of the observed radio source, but no firm conclusion has yet been drawn. Kronberg & Perry (1982) found an increased variance of the Faraday depth in conjunction with higher redshifts, as also found in some later studies (e.g. Welter et al. 1984; Kronberg et al. 2008). However, Oren & Wolfe (1995) did not find any evidence of an increase of the variance of the Faraday depth as a function of the redshift, as suggested also by the recent work by Hammond et al. (2012) and Pshirkov et al. (2015).

The rest of this paper is organized as follows. In § 2 we describe the theory behind our method. In § 3 the tests performed are presented, with predictions for the new generation of radio interferometers. Moreover, we outline a generalization of the algorithm in order to discriminate the contribution from different large-scale structures along the line of sight. Finally, in § 4 we draw our conclusions. The application of the algorithm to real data is left for future work, as explained in the text. In the following we adopt a Λ CDM cosmology with $H_0 = 67.3 \text{ km s}^{-1} \text{ Mpc}^{-1}$, $\Omega_m = 0.315$, $\Omega_\Lambda = 0.685$, and $\Omega_c = 0.0$ (Planck Collaboration 2014).

2. Theoretical framework

The probability for the extragalactic contribution, ϕ_e , along the line of sight, i , to take on a value within the infinitesimal interval between $\phi_{e,i}$ and $\phi_{e,i} + d\phi_{e,i}$ given the data, d , and a model parameterization, Θ , is given by the probability density distribution. In turbulent environments (see, e.g., Lawler & Dennison 1982; Tribble 1991; Feretti et al. 1995; Felten 1996, for galaxy clusters), this probability density distribution can be represented with a Gaussian. The mean and variance,

$$\langle \phi_{e,i} \rangle = \langle \phi_{e,i} \rangle_{(\phi_{e,i}|d,\Theta)} \quad (4)$$

$$\langle \phi_{e,i}^2 \rangle = \langle (\phi_{e,i} - \langle \phi_{e,i} \rangle_{(\phi_{e,i}|d)}) (\phi_{e,i} - \langle \phi_{e,i} \rangle_{(\phi_{e,i}|d)})^\dagger \rangle_{(\phi_{e,i}|d,\Theta)},$$

of this distribution are

$$\langle \phi_{e,i} \rangle = 0 \quad (5)$$

$$\langle \phi_{e,i}^2 \rangle = a_0^2 \int_0^{z_i} \int_0^{z_i} \frac{dl}{dz} \frac{dl'}{dz'} dz dz' \langle n(z) n(z') B_l(z) B_l(z') \rangle.$$

The zero mean results from the fact that we do not have any reason to suppose either a positive or a negative mean Faraday depth value. Frozen-in magnetic fields are expected to have strengths depending on redshift z . Because of the expansion of the Universe, lengths are stretched

$$\frac{l_0}{l} = (1+z). \quad (6)$$

In an isotropically expanding fluid with no significant fluctuations, the mean electron density evolves as

$$\frac{\langle n_e \rangle}{\langle n_0 \rangle} = (1+z)^3, \quad (7)$$

and, if the magnetic flux density is conserved, the magnetic field strength as

$$\frac{\langle B \rangle}{\langle B_0 \rangle} = \left(\frac{\langle n_e \rangle}{\langle n_0 \rangle} \right)^{\frac{2}{3}} = (1+z)^2, \quad (8)$$

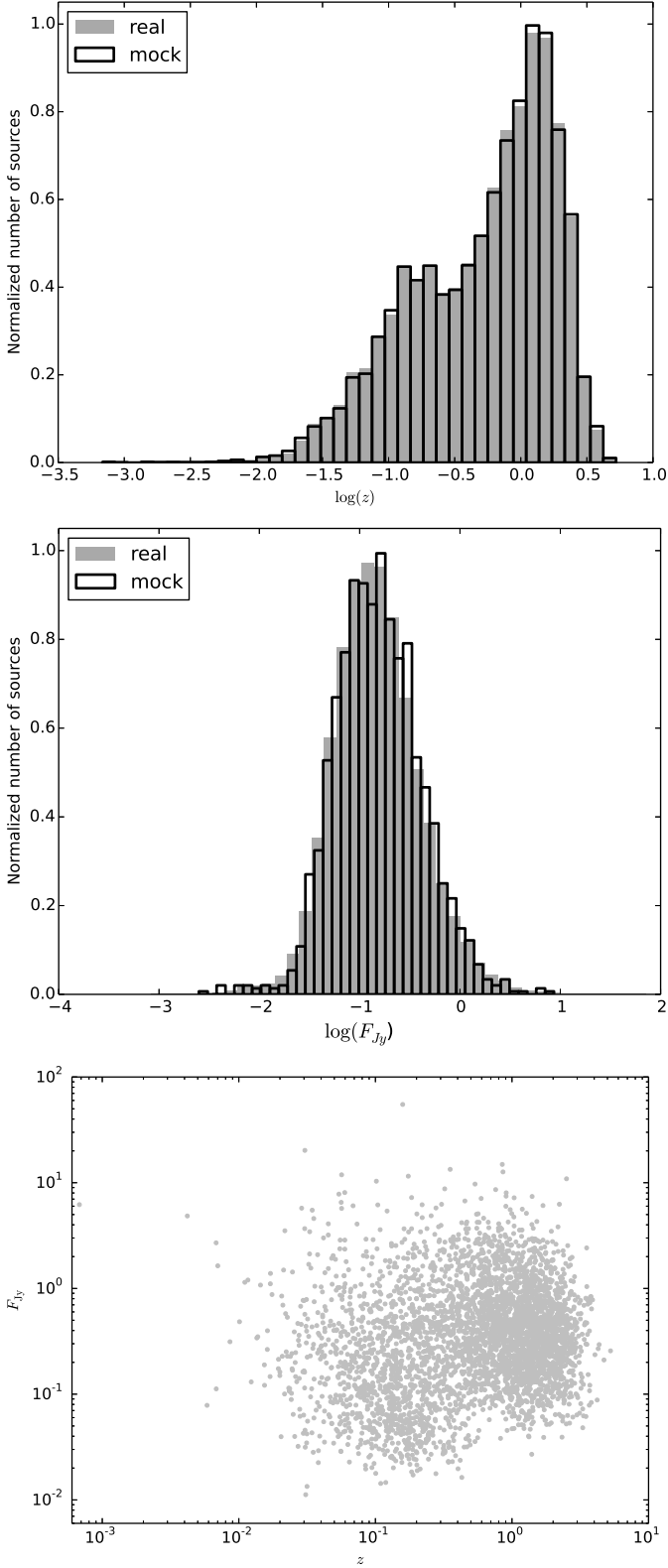


Fig. 1. Distribution of the real and mock sample of redshifts z (top), and flux densities F_{Jy} at 1.4 GHz (middle). In the bottom panel, flux density versus redshift for the sources with both measurements available (Taylor et al. 2009; Hammond et al. 2012).

where l_0 , $\langle n_0 \rangle$, and $\langle B_0 \rangle$ are the present-day values, and l , $\langle n_e \rangle$, and $\langle B \rangle$ are the values at the time when the signal was emitted by the source. If we consider these assumptions and we define a

length scale $\Lambda_l := \int dl' \langle B(l)B(l') \rangle / \langle B(l)^2 \rangle$, we obtain

$$\langle \phi_{e,i}^2 \rangle \approx a_0^2 \int_0^{z_i} \langle n_0^2 \rangle \langle B_{l_0}^2 \rangle \Lambda_{l_0} (1+z)^4 \frac{c}{H(z)} dz. \quad (9)$$

For the derivation of this expression see Appendix A. Here, we assumed an unstructured Universe and used the definition of proper displacement along a light-ray, $\frac{dl}{dz} = \frac{c}{(1+z)H(z)}$. Moreover, we assumed that, within a correlation length Λ_{l_0} , the redshift can be approximated to be constant. Magnetic field strength and structure as well as the electron density have different values in different environments, j . In the following, we assume them to depend only on the environment and not on the location within an environment. This simplification renders the problem feasible.

In this paper, as a first step, we will restrict our analysis to a two components (scenario 2C), the emitting radio source itself, whose contribution is $\sigma_{\text{int},i}^2(z_i, \Theta)$, and the medium between the source and the Galaxy, whose contribution is $\sigma_{\text{env},i}^2(z_i, \Theta)$, such that

$$\langle \phi_{e,i}^2 \rangle = \sigma_{e,i}^2(z_i, \Theta) = \sigma_{\text{int},i}^2(z_i, \Theta) + \sigma_{\text{env},i}^2(z_i, \Theta). \quad (10)$$

We denote with $\Theta = \{\sigma_{\text{int},0}, \sigma_{\text{env},0}, \chi_{\text{lum}}, \chi_{\text{red}}\}$ an N -dimensional vector, where N is the number of parameters used in the representation of the Faraday depth variance. These are the parameters we want to infer. We choose the following parameterization for the intrinsic contribution to the variance in Faraday depth,

$$\sigma_{\text{int},i}^2(z_i, \Theta) = \left(\frac{L_i}{L_0} \right)^{\chi_{\text{lum}}} \frac{\sigma_{\text{int},0}^2}{(1+z_i)^4} \quad (11)$$

where L_i is the luminosity¹ of the source i , $L_0 = 10^{27}$ W/Hz, and χ_{lum} absorbs possible dependencies on the luminosity of the source since faint sources may not be detected, and for the environmental contribution

$$\sigma_{\text{env},i}^2(z_i, \Theta) = \frac{D_i(z_i, \chi_{\text{red}})}{D_0} \sigma_{\text{env},0}^2, \quad (12)$$

where $D_0 = 1$ Gpc, and $D_i(z, \chi_{\text{red}})$ is defined as

$$D_i(z_i, \chi_{\text{red}}) = \int_0^{z_i} \frac{c}{H(z)} (1+z)^{4+\chi_{\text{red}}} dz, \quad (13)$$

to capture the redshift scaling of Eq. (9) as well as auxiliary modifications by the clumpiness of the Universe via χ_{red} . Since the length of the path covered by the signal in the source is unknown, we factored it in $\sigma_{\text{int},0}^2$ in Eq. (11). We note that $\sigma_{\text{int},0}$ and $\sigma_{\text{env},0}$ have been assumed to be independent of the redshift. In Eq. (11) the only redshift dependence is absorbed by the factor $(1+z_i)^{-4}$ that takes into account the effect of redshift on Faraday rotation (squared), while in Eq. (12) it is absorbed by $D_i(z_i, \chi_{\text{red}})$ which takes into account Eq. (13).

This parameterization describes the simplest scenario. For more complex scenarios that include three components, we refer to Appendix C, where we introduce an additional constant and latitude dependent term. Moreover, galaxies along the line of sight between a source and the observer can be responsible for high Faraday depth values (e.g. Kronberg & Perry 1982; Welter et al. 1984; Kronberg et al. 2008; Bernert et al. 2012), indicating magnetic field strengths in these intervening galaxies of $(1.8 \pm 0.4) \mu\text{G}$ (Farnes et al. 2014a). The rotation of the polarization angle due to these sources adds to that associated with the large-scale structure and, therefore, should be taken into account in a proper modeling. Since the aim of this paper is to give a proof of concept, we leave this for future work.

¹ This luminosity refers to the mean-frequency of the frequency band used for the computation of the Faraday depth values.

2.1. Bayesian inference

To constrain the vector $\Theta = \{\sigma_{\text{int},0}, \sigma_{\text{env},0}, \chi_{\text{lum}}, \chi_{\text{red}}\}$ on the basis of these data, d , we propose a Bayesian approach. The *posterior* probability distribution, $P(s|d)$, on a signal, s , after a dataset, d , is acquired, can be expressed with Bayes' theorem,

$$P(s|d) = \frac{P(d|s)P(s)}{P(d)}. \quad (14)$$

The *prior* probability distribution, $P(s)$, is modified by the data, d , through the *likelihood*, $P(d|s)$. The *evidence*, $P(d)$, is a normalization factor, obtained by marginalizing the joint probability, $P(d, s) = P(d|s)P(s)$, over all possible configurations of the signal, s .

In this context, the data, d , can be represented as a vector with elements d_i , with $i = 1, \dots, N_{\text{los}}$, where N_{los} is the total number of lines of sight. Each measurement, d_i , is the Faraday depth evaluated in the direction of the source, i , and is the result of the sum of a Galactic and an extragalactic contribution, $\phi_{g,i}$ and $\phi_{e,i}$, and the noise, n_i , of the measurement process, such that

$$d_i = \phi_{g,i} + \phi_{e,i} + n_i. \quad (15)$$

From the observed data, the Galactic foreground should be removed as well as possible to reveal the extragalactic contribution. However, any estimation of the Galactic foreground is based on the same data and is facing the separation problem for Galactic and extragalactic contributions. The only available discriminant (so far) is the large angular correlation the Galactic contribution shows. This allow for a statistical separation and Galactic model construction. Such a model will inevitably have uncertainties and correlations among such uncertainties, which have to be properly taken into account in a statistical search for extragalactic Faraday signals. To this end, Oppermann et al. (2012, 2015) developed a fully Bayesian approach to reconstruct the Galactic Faraday depth foreground and estimate the extragalactic contribution as well as the involved uncertainties by using the Faraday depth catalogs available to date. Their posterior for the extragalactic contribution can be used in order to further disentangle the intrinsic and environmental contributions. Oppermann et al. (2012, 2015)'s analysis relies on the assumption that for each source the prior knowledge can be described by a Gaussian probability density distribution,

$$P(\phi_e) = \prod_{i=1}^{N_{\text{los}}} \mathcal{G}(\phi_{e,i}, \sigma_e^2), \quad (16)$$

with a standard deviation, $\sigma_e \approx 7 \text{ rad m}^{-2}$, irrespective of the line of sight². Here, on the other hand, we want to test whether the variance is different for each line of sight, depending on the redshift of the source, according to Eq. (11) and Eq. (12). We note that in our approach the angular separation of sources is assumed to be large enough that the magnetic fields probed by different lines of sight can be modeled as uncorrelated. All angular correlations of Faraday depth on scales down to the effective resolution of the catalog ($\approx 0.5^\circ$), are absorbed by the Galactic component in this model. A more complete modeling would require to take into account possible correlations in the extragalactic component. Thus, our assumptions imply that the values derived with the proposed algorithm for the contributions of different environments to the Faraday depth dispersion are a lower limit.

² The notation $\mathcal{G}(x, X)$ indicates a one-dimensional Gaussian distribution for a variable x with zero mean and variance X .

We cannot follow the prescription described in Appendix D.2.3 of Oppermann et al. (2015) because our prior assumptions are too different from theirs. Instead, we resort to Gibbs sampling (Geman & Geman 1984; Wandelt et al. 2004). This approach relies on the fact that sampling from the conditional probability densities,

$$\phi_e \leftrightarrow P(\phi_e|\Theta, d), \quad (17)$$

and,

$$\Theta \leftrightarrow P(\Theta|\phi_e, d), \quad (18)$$

in a two-step iterative process is equivalent to drawing samples from the joint probability density

$$\phi_e, \Theta \leftrightarrow P(\Theta, \phi_e|d), \quad (19)$$

if the process is ergodic.

For the parameters $\sigma_{\text{int},0}$ and $\sigma_{\text{env},0}$ we choose a prior,

$$P(\sigma_{\text{int},0}, \sigma_{\text{env},0}) \propto \text{const.} \quad (20)$$

Results with other priors are discussed in Appendix D. Conversely, we do not expect the parameters χ_{lum} and χ_{red} to differ greatly from 0, since we have already accounted for all obvious redshift effects. This requirement is satisfied if we use the following Gaussian priors

$$P(\chi_{\text{lum}}, \chi_{\text{red}}) = \mathcal{G}(\chi_{\text{lum}}, 1) \mathcal{G}(\chi_{\text{red}}, 1), \quad (21)$$

and in combination

$$P(\Theta) = P(\sigma_{\text{int},0}, \sigma_{\text{env},0}) P(\chi_{\text{lum}}, \chi_{\text{red}}). \quad (22)$$

2.2. Description of the algorithm

Here, we describe the Gibbs sampling procedure mentioned in the previous section. We run the algorithm starting from values of the parameters Θ randomly drawn from their prior. This Θ vector is used to compute a variance for the prior of the extragalactic contribution,

$$P(\phi_e|\Theta) = \prod_{i=1}^{N_{\text{los}}} \mathcal{G}(\phi_{e,i}, \sigma_{e,i}^2(z_i, \Theta)), \quad (23)$$

where $\sigma_{e,i}^2(z_i, \Theta)$ is evaluated according to Eq. (10). A sample for the extragalactic contribution is drawn from the posterior

$$P(\phi_e|\Theta, d) = \frac{P(d|\phi_e, \Theta)P(\phi_e|\Theta)}{P(d|\Theta)}, \quad (24)$$

following the approach described in Oppermann et al. (2015), with the Galactic power spectrum, the Galactic profile, and the correction factors to the observed noise variance (indicated by η_i in the paper by Oppermann et al. 2015) fixed to the published values. After fixing the extragalactic sample, a new Θ sample is drawn from the conditional probability

$$P(\Theta|\phi_e) = \frac{P(\phi_e|\Theta)P(\Theta)}{P(\phi_e)} \propto \prod_{i=1}^{N_{\text{los}}} \mathcal{G}(\phi_{e,i}, \sigma_{e,i}^2(z_i, \Theta)) P(\Theta). \quad (25)$$

Here, we drop the dependence on the data, d , because Θ and d are conditionally independent given ϕ_e . To sample from this

Table 1. Mock catalogs. Col. 1: scenario considered for the generation of the mock catalog. Col. 2: identification code (ID) of the test. Col. 3: short description of the catalog. Col. 4: number of lines contained in the catalog. Col. 5: Observational uncertainty in Faraday depth. Col. 6: Figure where the results of the corresponding test are shown.

Scenario	ID	Description	los #	σ_{noise}^a (rad/m ²)	Figure
Two Component	2C1	Datasets used by Oppermann et al. (2012, 2015) ^b	41632	13.0	2(a)
	2C2	Datasets used by Oppermann et al. (2012, 2015) ^b	4003	13.0	2(b)
	NPC	LOFAR 120-160 MHz, North Polar Cap	2148	0.05	3(a,b)
	GW	LOFAR 120-160 MHz, Great Wall	1036	0.05	E.1
	POSSUM	ASKAP-POSSUM 1130-1430 MHz, South Polar Cap	3476	6.0	5
	B2SPC1	SKA Band 2, 0.65-1.67 GHz, South Polar Cap	3476	0.8	4(a,b)
	B2SPC2	SKA Band 2, 0.65-1.67 GHz, South Polar Cap	1129	0.8	F.2(b)
	B1SPC1	SKA Band 1, 0.35-1.05 GHz, South Polar Cap	3476	0.3	F.1(a,b)
	B1SPC2	SKA Band 1, 0.35-1.05 GHz, South Polar Cap	1129	0.3	F.2(a)
Three Component	3C1	Datasets used by Oppermann et al. (2012, 2015) ^b	41632	13.0	C.1(a)
	3C2	Datasets used by Oppermann et al. (2012, 2015) ^b	4003	13.0	C.1(b)
Latitude Dependence	LD1	Datasets used by Oppermann et al. (2012, 2015) ^b	41632	13.0	C.2(a)
	LD2	Datasets used by Oppermann et al. (2012, 2015) ^b	4003	13.0	C.2(b)
Prior 0	P0	Datasets used by Oppermann et al. (2012, 2015) ^b	41632	13.0	D.1(a)
Prior 1	P1	Datasets used by Oppermann et al. (2012, 2015) ^b	41632	13.0	D.1(b)

^a For present observations this value represents the mean value of the observed uncertainties. ^b The references for the surveys and catalogs used by Oppermann et al. (2012) are: Dennison (1979); Tabara & Inoue (1980); Simard-Normandin et al. (1981); Lawler & Dennison (1982); Rudnick & Jones (1983); Kato et al. (1987); Broten et al. (1988); Hennessy et al. (1989); Kim et al. (1991); Clegg et al. (1992); Wrobel (1993); Oren & Wolfe (1995); Minter & Spangler (1996); Condon et al. (1998); Gregorini et al. (1998); Vigotti et al. (1999); Clarke et al. (2001); Gaensler et al. (2001); Brown et al. (2003); Johnston-Hollitt (2003); Klein et al. (2003); Taylor et al. (2003); Clarke (2004); Johnston-Hollitt & Ekers (2004); Gaensler et al. (2005); McClure-Griffiths et al. (2005); Roy et al. (2005); Haverkorn et al. (2006); Brown et al. (2007); Braun et al. (2007); Mao et al. (2008); Feain et al. (2009); Heald et al. (2009); Taylor et al. (2009); Bonafede et al. (2010); Mao et al. (2010); Feain et al. (2011); Van Eck et al. (2011)

distribution we use a Metropolis-Hastings algorithm (Metropolis et al. 1953; Hasting 1970). When direct sampling is difficult, Metropolis-Hastings algorithms can approximate a probability distribution with random samples generated from the distribution itself. At each iteration a step in the parameter space is proposed according to a transition kernel and then accepted according to an acceptance function. If the proposed step is not accepted, the old Θ values are kept and used to draw a new sample of the extragalactic Faraday depths.

The convergence criteria adopted in this work are described in Appendix B.

3. Results

In the following we present tests performed with different Faraday depth catalogs. These catalogs differ in the number of components used to generate the overall extragalactic Faraday depth, the numbers of lines of sight in the sky, and the observational uncertainties that are different for the different radio surveys considered here. In Sect. 3.1 we demonstrate that the algorithm is working properly for the two-component scenario described in Sect. 2. In Sect. 3.2, we present the prospects with the surveys planned with the new generation of radio interferometers (LOFAR, ASKAP, and SKA).

We perform tests assuming an overall extragalactic Faraday depth in agreement with the values presently inferred, namely $\approx 7.0 \text{ rad m}^{-2}$ (Schnitzeler 2010; Oppermann et al. 2015), and comparable intrinsic and the environmental contributions. To satisfy these two requirements, we need to use slightly different values of the Θ parameters for surveys with different frequency specifications. Indeed, the contributions depend on the frequency through the luminosity of the source, see Eq. (11). Our choice of

the Θ parameters translates to a strength of magnetic fields intrinsic to the source of

$$\frac{\langle B_{l0} \rangle}{\mu\text{G}} \sim 0.5 \div 1 \left(\frac{\langle n_0 \rangle}{10^{-3} \text{ cm}^{-3}} \right)^{-1} \left(\frac{\Lambda_{l0}}{5 \text{ kpc}} \right)^{-1} \left(\frac{L}{100 \text{ kpc}} \right)^{-1}, \quad (26)$$

where L is the size of the emitting radio source, and to large scale magnetic field strengths of

$$\frac{\langle B_{l0} \rangle}{\text{nG}} \sim 2 \left(\frac{\langle n_0 \rangle}{10^{-5} \text{ cm}^{-3}} \right)^{-1} \left(\frac{\Lambda_{l0}}{5 \text{ Mpc}} \right)^{-1}. \quad (27)$$

In the tests for LOFAR, ASKAP, and SKA, we additionally consider an overall extragalactic Faraday rotation of $\approx 0.7 \text{ rad m}^{-2}$ to mimic weaker fields. This corresponds to magnetic field values weaker by a factor ten than those given in Eq. (26) and Eq. (27).

The two-component parameterization represents the simplest scenario. Nevertheless, the algorithm is able to successfully deal also with more complex scenarios that include a third constant or latitude-dependent component. These scenarios are discussed in Appendix C. Moreover, to assess if different priors can have an impact on our results, we consider in Appendix D a flat prior in σ^2 and a flat prior in $\ln(\sigma^2)$. In Table 1 we give a summary of all the setups we used, including those presented in the appendices. To each of them we assigned an identification code (ID), used in the paper to discriminate among the different scenarios. When the same collection of sources is used for tests with different values of the overall extragalactic Faraday depth, we distinguish among them by adding a roman letter. For example, Xa and Xb indicate tests performed using the collection of sources X and two different overall extragalactic Faraday depth standard deviation, a denotes $\approx 7.0 \text{ rad m}^{-2}$, while $b \approx 0.7 \text{ rad m}^{-2}$. In Table 2 we report all the values of the Θ parameters adopted in the different tests. In the main text we give both a quantitative and a visual

summary of the results of all the tests we performed, while the full posteriors are shown only for the most important tests we carried out. To make the reading easier, the posteriors for all the other tests are shown in the appendices.

3.1. Present-instrument observations

To assess the quality of the algorithm we generate a mock catalog for the sample of sources used by Oppermann et al. (2012, 2015). This mock catalog includes coordinates, redshifts, luminosities, and Faraday depth values.

The positions of the sources on the sky were kept the same as for the real sources. The majority (≈ 40000 sources) belong to the catalog of Taylor et al. (2009), and for 4003 of them, spectroscopic redshift measurements have been published by Hammond et al. (2012). For most of the sources, these catalogs give a flux density measurement that allows the computation of the luminosity of the source. Where available, we use the measured redshift and flux density. For the vast majority of the sources we generate a mock redshift, and for a few of them a mock flux density value. Mock redshifts and flux densities are extracted independently from the two observed distributions. In Fig. 1, the distribution of both the real and mock sample of redshifts and flux densities is shown respectively in the *top* and *middle* panel. In the *bottom* panel the observed flux density versus redshift distribution is presented. These two quantities appear to be weakly correlated. For sake of simplicity we neglected such correlation in our mock simulation, since it should not have any impact on our analysis. We assume all redshifts and luminosities to be known with negligible uncertainty.

For all the sources in the catalog we generate a mock Faraday depth value. The observed Faraday depth values consist of a Galactic, an extragalactic, and a noise contribution. We considered the Galactic contribution to be given by a sample extracted from the posterior of Oppermann et al. (2015). To mimic observational uncertainties, the noise variance has been computed for each source according to Eq. (37) in Oppermann et al. (2015), where as observed uncertainty, σ_i , we use the uncertainties reported in the observational catalogs and as η_i we use the values recovered by Oppermann et al. (2015). The observational error of each measurement has been extracted from a Gaussian with this standard deviation and zero-mean. Concerning the extragalactic contribution, in this test, we consider the 2C scenario described in § 2, namely an intrinsic and an environmental contribution,

$$\sigma_{e,i}^2(z_i, \Theta) = \left(\frac{L}{L_0}\right)^{\chi_{\text{lum}}} \frac{\sigma_{\text{int},0}^2}{(1+z_i)^4} + \frac{D_i(z_i)}{D_0} \sigma_{\text{env},0}^2. \quad (28)$$

The variances in Eq. (28) depend on the redshifts and luminosities of the sources. Therefore, each source will have a different variance. For each source, the extragalactic contribution is extracted from a Gaussian with this variance and zero mean. As summarized in Table 2, the contributions intrinsic to the source and to the medium between the source and the observer are respectively, $\tau_{\text{int},0} = 18.2 \text{ rad m}^{-2}$ and $\tau_{\text{env},0} = 1.4 \text{ rad m}^{-2}$. Since the mean of the factor $L_i/L_0/(1+z_i)^4$ is ≈ 0.06 and the mean of the factor D_i/D_0 is ≈ 15.5 , the standard deviation in the overall intrinsic and environmental components are $\sigma_{\text{int}}^{\text{true}} \approx 4.4 \text{ rad m}^{-2}$ and $\sigma_{\text{env}}^{\text{true}} \approx 5.3 \text{ rad m}^{-2}$. For this scenario, we run two tests corresponding to a different number of lines of sight:

- 41632 (2C1). This is the total number of lines of sight for which an estimate of the extragalactic contribution is available from Oppermann et al. (2015);

- 4003 (2C2). This number accounts for all the sources in the catalog 2C1 for which a redshift measurement is available as well (Hammond et al. 2012).

In Fig. 2 we show the results for the tests 2C1 and 2C2, meaning with a two-component scenario for 41632 lines of sight (a) and 4003 lines of sight (b). The histograms in the top plots of each column represent the 1-dimensional projection of the posterior for the corresponding parameter. The dotted lines mark the true value of the parameter. The dashed and dashed-dotted lines describe the posterior statistics, namely the mean and the 1σ confidence level respectively. The continuous lines indicate the prior used in our analysis. The panels in colors show the 2-dimensional projection of the posterior for a given couple of parameters. These plots show that our algorithm is able to recover the mock Θ -values for this scenario. The inferred posterior mean values agree well within the uncertainties with the correct ones and the posterior distributions are much narrower than the prior distributions. The dispersion in the parameters Θ increases by decreasing the number of lines of sight, as expected. The plots indicate that some of the parameters are correlated, e.g., most noticeably $\sigma_{\text{env},0} \cdot \chi_{\text{red}}$ that show a strong anticorrelation. This feature can be understood in light of Eq. (12). Indeed, for a given Faraday rotation σ_{env} associated with the structures between the source and the observer, larger $\sigma_{\text{env},0}$ imply smaller χ_{red} and vice versa. We expect the correlation in the posterior to be significant for any reasonable parameterization that allows for the same number of degrees of freedom.

In order to have a compact and complete visualization, in the rest of the paper we present all the tests we performed and their results as in Fig. 2.

3.2. Future prospects

We investigate the possibility to separate the Faraday rotation intrinsic to the emitting radio source from that due to the extragalactic environments between the source and the observer with the specifications of the SKA, its precursor, ASKAP, and its pathfinder, LOFAR. The mock rotation measure values for each source have been generated as described in Sect. 3.1. For each catalog the noise contribution has been extracted for each line of sight from a Gaussian with zero-mean and standard deviation equal to maximum uncertainty in Faraday depth expected in the corresponding frequency range, according to Stepanov et al. (2008). Luminosities at frequencies different from 1.4 GHz have been spectrally adjusted³.

Since our approach assumes that all the lines of sight are independent, i.e. sufficiently separated ($\gtrsim 1^\circ$) so that the cross-correlation function of their magnetic field is zero, in the following tests we compute the number of lines of sight considering a density of sources lower than or equal to one polarized source per square degree. The number of sources detected by ASKAP and SKA per square degree will be at least one hundred times larger. Here, we investigate if already with a small sample of lines of sight we would be able to put any constraints on the contribution from extragalactic large-scale environments, rather than exploit the information delivered by the full number of lines of sight and to show the full potential of ASKAP and SKA.

³ For convenience, we use a single power-law $F(\nu) \propto \nu^{-0.8}$, where $F(\nu)$ is the flux density.

3.2.1. LOFAR

We consider the LOFAR’s High Band Antennas (HBA) only, because of their better polarization performance. We select the HBA region of the spectrum with less contamination from radio frequency interference (120-160 MHz, Offringa et al. 2013). In this frequency range, the uncertainty on rotation measure values is expected to be $\leq 0.05 \text{ rad m}^{-2}$ for a signal-to-noise ratio larger than 5 (Stepanov et al. 2008). According to Mulcahy et al. (2014), the expected number of polarized extragalactic radio sources is 1 per 1.7 square degrees for 8 h-long observations, assuming an average degree of polarization of 1%, a spatial resolution of $20''$, and a detection threshold of $500 \mu\text{Jy}/\text{beam}/\text{rmsf}^4$ that corresponds to $S/N = 5$.

On the basis of these assumptions we generate coordinates in the sky for a collection of sources corresponding to a survey (8 h per pointing) in the direction of the North Polar Cap (NPC). Among these sources we select those with Galactic latitude larger than 55° . This results in approximately 2200 sources. We derive a catalog assuming an overall extragalactic Faraday rotation $\sigma_e \approx 7 \text{ rad m}^{-2}$ (NPCa), and one assuming an overall extragalactic Faraday rotation $\sigma_e \approx 0.7 \text{ rad m}^{-2}$ (NPCb). The results are shown in Fig. 3, respectively panel (a) and panel (b). These plots show that LOFAR can provide good constraints for both values of the overall extragalactic Faraday depth if a few thousand of lines of sight are used, with better performance for larger σ_e . The posterior distributions are much narrower than the prior distributions and the posterior means agree with the correct values within $1\text{--}2\sigma$. Tests performed with a smaller number of lines of sight are presented in Appendix E. These plots show that the algorithm performs well even for $N_{\text{los}} \approx 1000$ even if, as expected, the posterior distributions are wider.

3.2.2. SKA

The SKA is expected to observe the entire Southern sky with a spatial resolution of $2''$ and a sensitivity in polarization of $\approx 4 \mu\text{Jy}/\text{beam}$ (see, e.g., Johnston-Hollitt et al. 2015). The resulting sky grid of Faraday rotation values will be 200-300 times denser than the largest catalog available at the moment (see e.g. Hales 2013). The better resolution of $2''$, compared to the $45''$ of Taylor et al. (2009), will make it possible to identify optical counterparts uniquely and hence to assign a redshift estimate to a larger number of sources through spectroscopic follow-up observations. The *SKA1 Re-Baseline Design 2015* indicates the frequency bands 1, 2, and 5 as available on SKA_MID during SKA-Phase 1:

- band 1, 0.35–1.05 GHz;
- band 2, 0.65–1.67 GHz;
- band 5, 4.6–13.8 GHz.

In the following we consider the frequency range 0.65-1.67 GHz, since receivers in band 2 (B2) should be constructed first.

We produce mock Faraday depth values assuming a maximum standard deviation in the noise distribution of the rotation measure of 0.8 rad m^{-2} , according to Stepanov et al. (2008), for this frequency range and for $S/N > 5$. We generate a catalog of coordinates in the South Polar Cap (SPC) based on the assumption of one polarized source per square degree and we select those with Galactic latitude $b < -55^\circ$. This translates in $N_{\text{los}} \approx 3500$. We will refer to this catalog as B2SPC1. We produce catalogs of Faraday depth values assuming $\sigma_e \approx 7.0 \text{ rad m}^{-2}$ (B2SPC1a) and $\sigma_e \approx 0.7 \text{ rad m}^{-2}$ (B2SPC1b).

⁴ rmsf is the half-power width of the Faraday depth spread function.

In Fig. 4 we show the results for B2SPC1a and B2SPC1b, in panel (a) and (b) respectively. The plots for $\sigma_e \approx 7.0 \text{ rad m}^{-2}$ indicate that with $N_{\text{los}} \approx 3500$ we obtain a good disentangling of the environmental and intrinsic contributions, and their redshift and luminosity dependence, with narrow posterior distributions and mean values within $\approx 1\sigma$ from the true values. For the same amount of lines of sight but a smaller overall Faraday rotation $\sigma_e \approx 0.7 \text{ rad m}^{-2}$, the dispersion in $\sigma_{\text{env},0}$, χ_{lum} , and χ_{red} becomes broader but with mean values still within a few standard deviations from the assumed value. On the other hand, we do not get good constraints for the parameter $\sigma_{\text{int},0}$ that appears characterized by a large dispersion. For a better constraint of this parameter we would need to resort to a larger number of lines of sight. Since the sensitivity of the SKA will allow to detect hundreds of sources per square degree, narrower posterior distribution of the parameters can be obtained by increasing the number of lines of sight.

Because of the different number of lines of sight and different frequency bands we can not directly compare these results with the results for LOFAR. For an analysis of SKA performance at lower frequencies see Appendix F. In this appendix, results for SKA observations in band 1 as well as in band 2 but with a smaller number of lines of sight are shown. We do not consider frequency band 5. Even if moving to higher frequency sources have a higher degree of polarization, the maximum uncertainty in Faraday depth is larger and the total source counts reduce. Consequently, we expect that the parameters are poorly constrained if the same number of lines of sight is taken.

3.2.3. ASKAP

The *Polarisation Sky Survey of the Universe’s Magnetism* (POSSUM, Gaensler et al. 2010) is planned between 1130 and 1430 MHz with the Australian Square Kilometre Array Pathfinder (ASKAP). The survey will reach a sensitivity in U and Q of $< 10 \mu\text{Jy}/\text{beam}$ and a resolution of $10''$. This will result in a density of 70 polarized sources per square degree (Hales et al. 2014) and a Faraday depth catalog one hundred times denser than those currently existing (e.g., Taylor et al. 2009). To test the capabilities of this survey in constraining extragalactic magnetic fields, we use the same set-up described in Sect. 3.2.2, but with an uncertainty drawn from a Gaussian with $\sigma_{\text{noise}} = 6. \text{ rad m}^{-2}$. This should be a reliable approximation of the maximum uncertainty in Faraday depth for a polarized signal with a $S/N > 5$ (Stepanov et al. 2008). The results are shown in Fig. 5. ASKAP observations appear already quite promising for disentangling the contribution intrinsic to the source from that due to the large-scale environments for $\sigma_e \approx 7.0 \text{ rad m}^{-2}$, already if Faraday depth values are available only for one source per square degree. The dispersion in the parameters is larger than that derived in Sect. 3.2.2 for the same collection of sources and overall extragalactic Faraday variance (Fig. 4a), as expected being the maximum uncertainty in Faraday depth larger. However, the mean values of the posterior agree within at most about 1σ with the true values.

3.3. Discussion

We developed a Bayesian algorithm to disentangle extragalactic contributions in the Faraday depth signal. It builds upon an algorithm to reconstruct the Galactic Faraday screen and its uncertainty-correlation structure previously presented by Oppermann et al. (2015). We tested the algorithm by modeling the

overall extragalactic contribution as the sum of an intrinsic and an environmental component, as described in Sect. 3.1, but see Appendix C for the inclusion of a constant or a latitude dependent term. These tests show that the algorithm is able to discriminate among the different components and their dependence on the luminosity and the redshift of the source, if a suitable number of lines of sight is available.

For test purposes, we built mock catalogs according to the specifications of the catalogs available in the literature after correcting for poorly known uncertainty information (see Sect. 3.1). The results in Fig. 2(b) indicate that by applying the algorithm to the currently available dataset we could already infer preliminary information about extragalactic magnetic fields, if a few thousands of sources with reliable observational uncertainty were available. For the 4003 sources in Fig. 2(b), indeed, redshift and flux density values are available. Nevertheless, since actually we do not consider all their Faraday depth noise variances to be reliable (see Appendix A of Oppermann et al. 2015), and the applied correction factors, η_i , are only statistical estimates, we would need to additionally sample in the η_i -parameter space in order to use the algorithm with real data, as described by Oppermann et al. (2015). The modern techniques of analysis, such as model fitting of the fractional polarization components q and u (e.g., Farnsworth et al. 2011; Ideguchi et al. 2014), rotation measure synthesis (e.g., Brentjens & de Bruyn 2005; Akahori et al. 2014b) and Faraday synthesis (Bell & Enßlin 2012), and the future radio surveys will partially overcome this problem. The large bandwidth of the new radio interferometer will allow to reduce the risk of $m\pi$ -ambiguity, particularly strong when the λ^2 -fit approach is used, as well as to reach a sufficiently high resolution in Faraday depth to distinguish nearby Faraday components. We note that when the distance between two peaks in a Faraday spectrum is smaller than the resolution, the uncertainty in the Faraday depth may be driven by the Faraday point spread function (e.g., Farnsworth et al. 2011; Farnes et al. 2014b; Kumazaki et al. 2014). For these reasons, the catalogs coming from Faraday depth grids planned with LOFAR, ASKAP, and the SKA will be more reliable both in terms of Faraday depth values and of uncertainties. Therefore, we investigated the prospects of these simpler future datasets here and address the more complex application of our technique to present data in a separate work. We assumed the computation to be dominated by the uncertainties in the Faraday depth estimates for each source, while the coordinates, luminosities and redshifts to be exactly known. With the advent of highly-accurate Faraday depth catalogs, this may change and in future work we will need to investigate to what depths and accuracy redshifts, and luminosities are needed in order to apply the method we propose. This is particularly important for redshifts. Indeed, the catalog used in this work reports a spectroscopic redshift for each source (Hammond et al. 2012). Recently, optical surveys, such as 2MASS, WISE, and SuperCOSMOS, have measured the photometric redshifts for millions of galaxies up to $z \approx 0.5$ (e.g. Bilicki et al. 2014), and the surveys planned with the next generation of telescopes will further increment this number. Nevertheless, photometric redshifts are less accurate than spectroscopic redshifts. This will require to evaluate the impact of their uncertainties on our results.

Our tests indicate that LOFAR, ASKAP, and the SKA will allow us to infer information about cosmological magnetic fields already with a few thousands of lines of sight, with better performance when lower frequencies are used. We want to stress that the uncertainties used in our tests only represent statistical uncertainties and any systematic issues have been neglected. In principle, LOFAR observations could be already used for this

aim but the development of a pipeline for the reduction of polarization data is still in progress. The enhanced capabilities of the Jansky Very Large Array (JVLA) make the new centimeter-wavelength sky survey (VLASS, <https://science.nrao.edu/science/surveys/vlass>) planned with this instrument a good opportunity for the application of this algorithm and for delivering significant results in the study of cosmic magnetism already in the next years.

In Table 2 we give a quantitative summary of the results. For each test we report the true values τ of the Θ parameters which describe the intrinsic and environmental contribution to the Faraday depth, their mean values μ , and their uncertainties σ , as well as the displacement of the mean from the true value in terms of the uncertainty,

$$\epsilon = \left| \frac{\mu - \tau}{\sigma} \right|. \quad (29)$$

These values have been computed after discarding the burn-in samples by visual inspection. The comparison of the results obtained with the mock catalogs created for present instruments 2C1 and 2C2 indicates that by increasing the number of sources with known redshift by a factor ten, the uncertainty in the Θ parameters can be reduced by about a factor two. This would no longer be valid if the sources without redshift information represent a different population than the observed one, since in our test we adopted mock values for these sources randomly extracted from the observed redshift distribution. A similar result is obtained if the observational uncertainty σ_{noise} is reduced by approximately a factor ten, as shown by the comparison of results corresponding to catalog 2C2 and the SKA catalog B2SPC1a. These two tests refer to a similar number of lines of sight and to a similar frequency range⁵. In Fig. 6 we present a visual summary of the results for all the two- and three-component scenarios corresponding to an overall extragalactic Faraday rotation of approximately both 7 rad m^{-2} (left panels) and 0.7 rad m^{-2} (right panels) for the four parameters $\sigma_{\text{int},0}$, $\sigma_{\text{env},0}$, χ_{lum} , and χ_{red} . The uncertainty on the parameters Θ decreases by increasing the number of lines of sight, N_{los} , and by decreasing the observational error, σ_{noise} . The best results are obtained when a good compromise between these two numbers is used, as for example shown by the scenarios NPCa and NPCb. Nevertheless, the comparison of the results of tests corresponding to different instruments can be not straightforward because they refer to different frequency bands and to slightly different values of the Θ parameters.

The problem we are tackling is characterized by different complexities. We are looking for a very weak signal, by using the residual information left in the data after the Galactic contribution has been derived. At the same time, we expect this signal to be characterized by a possible redshift dependence, even if very weak since not yet detected, and by cross-correlations of the extragalactic magnetic field along different lines of sight. In this work we try to address the first two issues with a Bayesian approach able to properly combine all the available observational information and allowing for a redshift dependence in our model. On one hand, we might overestimate the extragalactic contributions, since we are not including an uncorrelated Galactic component in the model. This term can be easily included in our algorithm, as shown by the tests in Appendix C, and quantified with real data. On the other hand, we do not take into account

⁵ Indeed, the 2C2-sources all belong to the catalog by Taylor et al. (2009), therefore their noise uncertainties refer to the frequency range 1365-1435 MHz.

a possible correlated component of the extragalactic magnetic field, which if present would be beneficial for our analysis. This means that the magnetic field values that can be inferred have to be considered rather as a lower limit, even if we expect this error to be small (e.g., Akahori & Ryu 2011). This is not a problem for surveys performed with LOFAR, since the expected density of extragalactic polarized sources is lower than the density of sources we assume. On the contrary, with ASKAP and the SKA, we will be able to detect at least one hundred sources per square degree. An approach to deal with possible cross-correlations between lines of sight is being developed with the intention to apply this new technique to forthcoming ultra-deep JVLA observations from the CHILES Con Pol survey (Hales et al. in preparation). The combination of the two methods would allow to exploit in an optimal way the information coming from the denser grids of Faraday depth measurements provided by SKA and ASKAP surveys.

Finally, we stress that the aim of this paper is to give a proof of concept. Indeed, the present version of the algorithm requires a high computational burden that limits its efficiency. For example, the time required to run a test on our computer cluster is of the order of a couple of months per chain even when only a few thousands lines of sight are considered. We are currently working on performance optimization to make the algorithm suitable to be applied to the upcoming large Faraday depth catalogs.

3.4. Future developments

The work presented in this paper prepares a Bayesian technique to investigate of magnetic fields in the large-scale structure, in particular in filaments and voids. As a next step we want to discriminate among the amount of Faraday rotation due to each large scale structure environment (see also Vacca et al. 2015). When different large-scale environments are considered, the variance in the extragalactic Faraday rotation can be parameterized as

$$\langle \phi_{e,i}^2 \rangle \approx a_0^2 \int_0^{z_i} \langle n_0^2 \rangle \langle B_{l_0}^2 \rangle \Lambda_{l_0} (1+z)^4 \frac{c}{H(z)} dz$$

$$\approx \left[\left(\frac{L_i}{L_0} \right)^{\chi_{lum}} \frac{\sigma_{int,0}^2}{(1+z_i)^4} + \sum_{j=1}^{N_{env}} l_{ij} \sigma_j^2 \right], \quad (30)$$

where $\sigma_1, \sigma_2, \dots, \sigma_{N_{env}}$ are the contributions from N_{env} different environments and l_{ij} is the length of the line of sight, i , through each environment, j .

With a Bayesian approach, Jasche et al. (2010) (see also Leclercq et al. 2015) reconstructed the cosmic density field. They used optical data from the SDSS *Data Release 7* (Abazajian et al. 2009) and classified the structures as voids, sheets, filaments, and galaxy clusters, according to the classification scheme of Hahn et al. (2007). This reconstruction enables us to compute the path covered by the radio signal through each environment, i.e., the elements l_{ij} in Eq. (30), once the position of the radio source is identified by using the redshift. This posterior of the large scale structure density field is available in the form of samples. Radio sources can belong to different environments (e.g. galaxy clusters and filaments) and the path covered by the signal in each environment differs for each radio source. These facts can be statistically taken into account with the use of a collection of sources distributed over all the sky and of different realizations of the large scale structure. We plan to use the full posterior of the large scale structure in order to statistically estimate which is the amount of variance due to the different types of environments in the observed Faraday depths.

4. Conclusions

The properties of cosmic magnetic fields constitute outstanding questions in modern cosmology. To get a better understanding it is essential to shed light on the properties of magnetic fields in large-scale environments, meaning filaments and voids, where turbulent intracluster gas motions have not yet enhanced the magnetic field and, consequently, the magnetic field strength and structure still depend on the seed field power spectrum.

Upcoming generations of radio telescopes, first LOFAR, and in the next decades the SKA, will perform polarization sky surveys with high sensitivity. Modern techniques based on rotation measure synthesis and Faraday synthesis, will enable us to perform a proper analysis of the polarization properties of extragalactic radio sources, thus providing unprecedented, highly accurate Faraday depth catalogs in frequency ranges from a few hundreds MHz to a few GHz. A statistical approach is required to exploit the information encoded in these data. For this reason we developed a Bayesian algorithm able to combine radio observations with luminosities and redshifts of sources, aiming at disentangling contributions to the extragalactic Faraday rotation intrinsic to radio sources and due to the large-scale structure, and in this way infer information about large-scale magnetic fields. Knowledge of the redshift is essential in this approach. The present all-sky photometric optical surveys and the surveys planned with the next generation of telescopes will greatly enlarge the number of sources for which this information will be available.

The work described in this paper is a proof of concept and shows that our algorithm can be used to discriminate between the Faraday depth generated by the radio source itself and the contribution due to the large-scale structures. Additionally, our algorithm is able to investigate the dependence of these terms on the redshift and the radio luminosity of the sources. The tests performed with mock LOFAR, ASKAP, and SKA data suggest that this technique is promising for the investigation of magnetic fields with strengths of a few μG down to a few nG, when uncertainties in the data are up to a few rad m^{-2} and known with high accuracy. We note that our modeling does not take into account any correlated component of extragalactic magnetic fields. Consequently inferred magnetic field strengths have to be considered as a lower limit.

The main characteristics of upcoming polarization surveys can be summarized by the number of lines of sights and by the maximum observational uncertainty in Faraday depth. Our tests indicate that, for a given number of lines of sight, better constraints can be obtained with observations at lower frequencies, because of the smaller observational uncertainty. Therefore, in principle, LOFAR and, thanks to its higher sensitivity even more, SKA_LOW (50–350 MHz) observations would be ideal. Nevertheless, the scant number of polarized sources at these frequencies and the difficulties in the calibration of the data could make the use of these data complex. ASKAP and SKA_MID observations respectively in the frequency range 1130–1430 MHz and 650–1670 MHz appear to be promising as well. We should be able to put useful constraints on large scale magnetic fields already with Faraday depth measurements for a few thousands of sources, and improve their determination by increasing the number of lines of sight. An increment in the number of lines of sight by a given factor reduces the uncertainty in the estimation of the intrinsic and environmental contribution as a reduction by the same factor in the observational uncertainty does, indicating that deeper observations of small fields could be a valuable or even better alternative to all sky surveys.

We are aware that many aspects of our approach require improvements: e.g., computational efficiency, inclusion of a correlated extragalactic magnetic field component, and of uncertainty in redshift, etc. Nevertheless, we present a first step toward a Bayesian study of magnetic fields associated with the cosmic large-scale structures.

Acknowledgments

VV thanks Federica Govoni, Mark Birkinshaw, Matteo Murgia, and Gabriele Giovannini for useful discussions. The implementation of the code makes use of the NIFTY package by Selig et al. (2013) and of the cosmology calculator by Ned Wright (www.astro.ucla.edu/~wright). This research was supported by the DFG Forschungsguppe 1254 “Magnetisation of Interstellar and Intergalactic Media: The Prospects of Low-Frequency Radio Observations”. K.T. is supported by Grant-in-Aid from the Ministry of Education, Culture, Sports, Science and Technology (MEXT) of Japan, Nos. 24340048 and 26610048. TS and HR acknowledge support from the ERC Advanced Investigator programme NewClusters 321271.

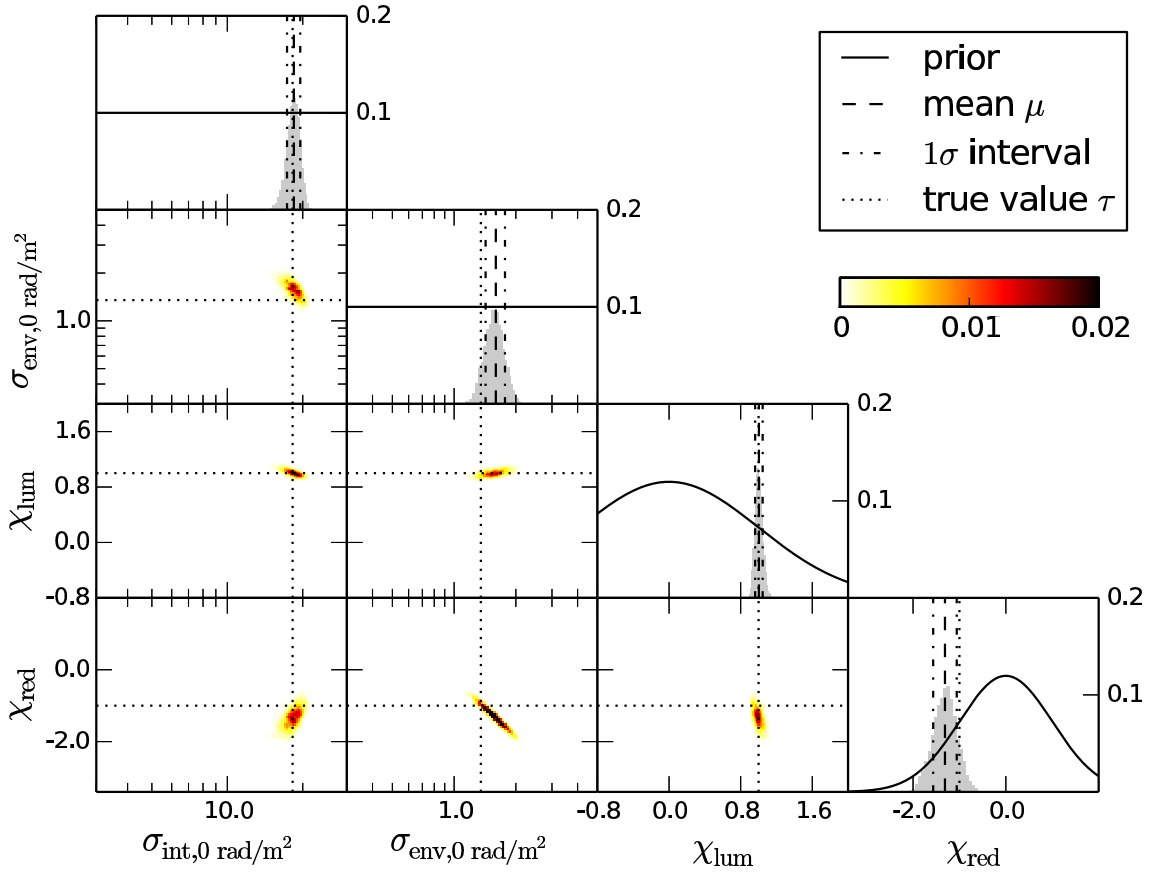
References

- Abazajian, K. N., Adelman-McCarthy, J. K., Agüeros, M. A., et al. 2009, *ApJS*, 182, 543
- Akahori, T., & Ryu, D. 2011, *ApJ*, 738, 134
- Akahori, T., Gaensler, B. M., & Ryu, D. 2014a, *ApJ*, 790, 123
- Akahori, T., Kumazaki, K., Takahashi, K., & Ryu, D. 2014b, *PASJ*, 66, 65
- Bagchi, J., Enßlin, T. A., Miniati, F., et al. 2002, *New A*, 7, 249
- Bell, M. R., & Enßlin, T. A. 2012, *A&A*, 540, A80
- Bernet, M. L., Miniati, F., & Lilly, S. J. 2012, *ApJ*, 761, 144
- Bilicki, M., Peacock, J. A., Jarrett, T. H., Cluver, M. E., & Steward, L. 2014, *arXiv:1408.0799*
- Bonafede, A., Feretti, L., Murgia, M., et al. 2010, *A&A*, 513, A30
- Braun, R., Oosterloo, T. A., Morganti, R., Klein, U., & Beck, R. 2007, *A&A*, 461, 455
- Brentjens, M. A., & de Bruyn, A. G. 2005, *A&A*, 441, 1217
- Broderick, A. E., Pfrommer, C., Puchwein, E., Chang, P., & Smith, K. M. 2014a, *ApJ*, 796, 12
- Broderick, A. E., Pfrommer, C., Puchwein, E., & Chang, P. 2014b, *ApJ*, 790, 137
- Brooks, S. P. & Gelman, A. 1997, “General Methods for Monitoring Convergence of Iterative Simulations”, *Journal of Computational and Graphical Statistics*, 7, 434–455
- Brotten, N. W., MacLeod, J. M., & Vallee, J. P. 1988, *Ap&SS*, 141, 303
- Brown, J. C., Taylor, A. R., & Jackel, B. J. 2003, *ApJS*, 145, 213
- Brown, J. C., Haverkorn, M., Gaensler, B. M., et al. 2007, *ApJ*, 663, 258
- Burn, B. J. 1966, *MNRAS*, 133, 67
- Carilli, C. L., & Taylor, G. B. 2002, *ARA&A*, 40, 319
- Clarke, T. E., Kronberg, P. P., Böhringer, H. 2001, *ApJL*, 547, L111
- Clarke, T. E. 2004, *Journal of Korean Astronomical Society*, 37, 337
- Clegg, A. W., Cordes, J. M., Simonetti, J. M., & Kulkarni, S. R. 1992, *ApJ*, 386, 143
- Condon, J. J., Cotton, W. D., Greisen, E. W., et al. 1998, *AJ*, 115, 1693
- Dennison, B. 1979, *AJ*, 84, 725
- Donnert, J., Dolag, K., Lesch, H., Müller, E. 2009, *MNRAS*, 392, 1008
- Enßlin, T. A., Frommert, M., & Kitaura, F. S. 2009, *PhRvD*, 80, 105005
- Farnes, J. S., O’Sullivan, S. P., Corrigan, M. E., & Gaensler, B. M. 2014a, *ApJ*, 795, 63
- Farnes, J. S., Gaensler, B. M., & Carretti, E. 2014b, *ApJS*, 212, 15
- Farnsworth, D., Rudnick, L., & Brown, S. 2011, *AJ*, 141, 191
- Feain, I. J., Ekers, R. D., Murphy, T., et al. 2009, *ApJ*, 707, 114
- Feain, I. J., Cornwell, T. J., Ekers, R. D., et al. 2011, *ApJ*, 740, 17
- Felten, J. E. 1996, *Clusters, Lensing, and the Future of the Universe*, 88, 271
- Feretti, L., Dallacasa, D., Giovannini, G., & Tagliani, A. 1995, *A&A*, 302, 680
- Feretti, L., Giovannini, G., Govoni, F., & Murgia, M. 2012, *A&A Rev.*, 20, 54
- Gaensler, B. M., Dickey, J. M., McClure-Griffiths, N. M., et al. 2001, *ApJ*, 549, 959
- Gaensler, B. M., Haverkorn, M., Staveley-Smith, L., et al. 2005, *Science*, 307, 1610
- Gaensler, B. M., Landecker, T. L., Taylor, A. R., & POSSUM Collaboration 2010, *Bulletin of the American Astronomical Society*, 42, #470.13
- Gelman, A., & Rubin, D. B. 1992, “Inference from Iterative Simulation Using Multiple Sequences”, *Statistical Science*, 7, 457–472
- Geman, S., & Geman, D. 1984, *IEEE Transactions on Pattern Analysis and Machine Intelligence*, 6, 721
- Giovannini, G., Vacca, V., Girardi, M., et al. 2013, *MNRAS*, 435, 518
- Giovannini, G., Bonafede, A., Brown, S., et al. 2015, *Advancing Astrophysics with the Square Kilometre Array (AASKA14)*, 104
- Govoni, F., & Feretti, L. 2004, *International Journal of Modern Physics D*, 13, 1549
- Gott, J. R., III, Jurić, M., Schlegel, D., et al. 2005, *ApJ*, 624, 463
- Gregorini, L., Vigotti, M., Mack, K.-H., Zoenchen, J., & Klein, U. 1998, *A&AS*, 133, 129
- Hahn, O., Porciani, C., Carollo, C. M., & Dekel, A. 2007, *MNRAS*, 375, 489
- Hales, C. A. 2013, *arXiv:1312.4602*
- Hales, C. A., Norris, R. P., Gaensler, B. M., & Middelberg, E. 2014, *MNRAS*, 440, 3113
- Hammond, A. M., Robishaw, T., & Gaensler, B. M. 2012, *arXiv:1209.1438*
- Hennessy, G. S., Owen, F. N., & Eilek, J. A. 1989, *ApJ*, 347, 144
- Harris, D. E., Stern, C. P., Willis, A. G., & Dewdney, P. E. 1993, *AJ*, 105, 769
- Hastings, W. K. 1970, *Biometrika*, 57, 1
- Haverkorn, M., Gaensler, B. M., McClure-Griffiths, N. M., Dickey, J. M., & Green, A. J. 2006, *ApJS*, 167, 230
- Heald, G., Braun, R., & Edmonds, R. 2009, *A&A*, 503, 409
- Ichiki, K., Takahashi, K., Ohno, H., Hanayama, H., & Sugiyama, N. 2006, *Science*, 311, 827
- Ideguchi, S., Takahashi, K., Akahori, T., Kumazaki, K., & Ryu, D. 2014, *PASJ*, 66, 5
- Jasche, J., Kitaura, F. S., Li, C., & Enßlin, T. A. 2010, *MNRAS*, 409, 355
- Johnston-Hollitt, M. 2003, *Ph.D. Thesis*
- Johnston-Hollitt, M., & Ekers, R. D. 2004, *arXiv:astro-ph/0411045*
- Johnston-Hollitt, M. et al. 2015, “Using the Rotation Measure Grid to Reveal the Mysteries of the Magnetised Universe”, in proceedings of “Advancing Astrophysics with the Square Kilometre Array”, *PoS(AASKA14)092*
- Kato, T., Tabara, H., Inoue, M., & Aizu, K. 1987, *Nature*, 329, 223
- Kim, K.-T., Tribble, P. C., & Kronberg, P. P. 1991, *ApJ*, 379, 80
- Klein, U., Mack, K.-H., Gregorini, L., & Vigotti, M. 2003, *A&A*, 406, 579
- Kronberg, P. P., & Perry, J. J. 1982, *ApJ*, 263, 518
- Kronberg, P. P., Kothes, R., Salter, C. J., & Perillat, P. 2007, *ApJ*, 659, 267
- Kronberg, P. P., Bernet, M. L., Miniati, F., et al. 2008, *ApJ*, 676, 70
- Kumazaki, K., Akahori, T., Ideguchi, S., Kurayama, T., & Takahashi, K. 2014, *PASJ*, 66, 61
- Lawler, J. M., & Dennison, B. 1982, *ApJ*, 252, 81
- Leclercq, F., Jasche, J., & Wandelt, B. 2015, *A&A*, 576, L17
- Mao, S. A., Gaensler, B. M., Stanimirović, S., et al. 2008, *ApJ*, 688, 1029
- Mao, S. A., Gaensler, B. M., Haverkorn, M., et al. 2010, *ApJ*, 714, 1170
- McClure-Griffiths, N. M., Dickey, J. M., Gaensler, B. M., et al. 2005, *ApJS*, 158, 178
- Metropolis, N., Rosenbluth, A. W., Rosenbluth, M. N., Teller, A. H., & Teller, E. 1953, *Journal of Chemical Physics*, 21, 6
- Minter, A. H., & Spangler, S. R. 1996, *ApJ*, 458, 194
- Mulcahy, D. D., Horneffer, A., Beck, R., et al. 2014, *A&A*, 568, AA74
- Neronov, A., & Vovk, I. 2010, *Science*, 328, 73
- Offringa, A. R., de Bruyn, A. G., Zaroubi, S., et al. 2013, *A&A*, 549, AA11
- Oppermann, N., Junklewitz, H., Robbers, G., et al. 2012, *A&A*, 542, A93
- Oppermann, N., Junklewitz, H., Greiner, M., et al. 2015, *A&A*, 575, A118
- Oren, A. L., & Wolfe, A. M. 1995, *ApJ*, 445, 624
- Planck Collaboration, Ade, P. A. R., Aghanim, N., et al. 2014, *A&A*, 571, AA16
- Planck Collaboration, Ade, P. A. R., Aghanim, N., et al. 2015, *arXiv:1502.01594*
- Shirkov, M. S., Tinyakov, P. G., & Urban, F. R. 2015, *arXiv:1504.06546*
- Roy, S., Rao, A. P., & Subrahmanyam, R. 2005, *MNRAS*, 360, 1305
- Rudnick, L., & Jones, T. W. 1983, *AJ*, 88, 518
- Schnitzler, D. H. F. M. 2010, *MNRAS*, 409, L99
- Selig, M., Bell, M. R., Junklewitz, H., et al. 2013, *A&A*, 554, A26
- Simard-Normandin, M., Kronberg, P. P., & Button, S. 1981, *ApJS*, 45, 97
- Staszyn, F., Nuza, S. E., Dolag, K., Beck, R., & Donnert, J. 2010, *MNRAS*, 408, 684
- Stepanov, R., Arshakian, T. G., Beck, R., Frick, P., & Krause, M. 2008, *A&A*, 480, 45
- Tabara, H., & Inoue, M. 1980, *A&AS*, 39, 379
- Takahashi, K., Ichiki, K., Ohno, H., & Hanayama, H. 2005, *Physical Review Letters*, 95, 121301
- Takahashi, K., Mori, M., Ichiki, K., & Inoue, S. 2012, *ApJ*, 744, L7
- Takahashi, K., Mori, M., Ichiki, K., Inoue, S., & Takami, H. 2013, *ApJ*, 771, L42
- Tavecchio, F., Ghisellini, G., Foschini, L., et al. 2010, *MNRAS*, 406, L70
- Taylor, A. R., Gibson, S. J., Peracaula, M., et al. 2003, *AJ*, 125, 3145
- Taylor, A. R., Stil, J. M., & Sunstrum, C. 2009, *ApJ*, 702, 1230
- Tribble, P. C. 1991, *MNRAS*, 250, 726
- Vacca, V., Oppermann, N., Enßlin, T., et al. 2015, *arXiv:1501.00415*
- Vallée, J. P., MacLeod, M. J., & Brotten, N. W. 1986, *A&A*, 156, 386
- Van Eck, C. L., Brown, J. C., Stil, J. M., et al. 2011, *ApJ*, 728, 97
- Vigotti, M., Gregorini, L., Klein, U., & Mack, K.-H. 1999, *A&AS*, 139, 359
- Wandelt, B. D., Larson, D. L., & Lakshminarayanan, A. 2004, *Phys. Rev. D*, 70, 083511
- Welter, G. L., Perry, J. J., & Kronberg, P. P. 1984, *ApJ*, 279, 19
- Wrobel, J. M. 1993, *AJ*, 106, 444
- Xu, H., Li, H., Collins, D. C., Li, S., & Norman, M. L. 2010, *ApJ*, 725, 2152
- Xu, H., Li, H., Collins, D. C., Li, S., & Norman, M. L. 2011, *ApJ*, 739, 77

Table 2. In Col. 1 the Identification code (ID) of the catalog is displayed. In the rest of the columns the true value τ , the mean μ , the uncertainty σ , and the displacement ϵ between mean and true value in terms of uncertainty is given. In the last column the standard deviation in the total extragalactic Faraday depth σ_e is reported.

ID	τ	$\sigma_{\text{int},0}$	ϵ	τ	$\sigma_{\text{env},0}$	ϵ	τ	$\sigma_{\text{c}/\text{lat}}$	ϵ	τ	χ_{lum}	ϵ	τ	χ_{red}	ϵ	σ_e
		$\mu \pm \sigma$			$\mu \pm \sigma$			$\mu \pm \sigma$			$\mu \pm \sigma$			$\mu \pm \sigma$		rad m^{-2}
2C1	18.2	18.4 \pm 1.1	0.2	1.4	1.6 \pm 0.2	1.5				1.0	1.0 \pm 0.04	0.0	-1.0	-1.3 \pm 0.3	1.2	≈ 7.0
2C2	18.2	19.1 \pm 2.5	0.3	1.4	1.3 \pm 0.4	0.1				1.0	0.9 \pm 0.1	0.7	-1.0	-0.7 \pm 0.6	0.4	
3C1	16.5	14.5 \pm 1.2	1.6	1.1	1.2 \pm 0.2	0.7		4.2 \pm 0.3	1.2	1.0	1.1 \pm 0.1	1.5	-1.0	-1.1 \pm 0.3	0.2	
3C2	16.5	11.1 \pm 3.6	1.5	1.1	1.8 \pm 0.5	1.6	3.9	4.0 \pm 0.7	0.2	1.0	1.1 \pm 0.3	0.4	-1.0	-1.7 \pm 0.6	1.2	
LD1	16.5	17.2 \pm 1.1	0.6	1.1	1.1 \pm 0.2	0.2	0.58	0.56 \pm 0.04	0.5	1.0	1.0 \pm 0.04	0.0	-1.0	-1.1 \pm 0.4	0.2	
LD2	16.5	15.6 \pm 2.7	0.3	1.1	1.1 \pm 0.4	0.03	0.58	0.7 \pm 0.1	0.9	1.0	1.0 \pm 0.1	0.3	-1.0	-1.1 \pm 0.8	0.1	
GW	8.6	9.5 \pm 0.7	1.2	1.4	1.0 \pm 0.2	1.8				0.9	0.8 \pm 0.1	1.2	-1.0	-0.1 \pm 0.5	1.6	
NPCa	8.6	7.4 \pm 0.7	1.7	1.4	1.6 \pm 0.2	0.9				0.9	1.0 \pm 0.1	1.4	-1.0	-1.3 \pm 0.3	0.9	
POSSUM	18.2	16.9 \pm 1.8	0.8	1.4	1.5 \pm 0.3	0.5				1.0	1.0 \pm 0.1	0.2	-1.0	-1.1 \pm 0.4	0.3	
B2SPC1a	18.2	18.9 \pm 0.9	0.7	1.4	1.2 \pm 0.1	0.9				1.0	1.0 \pm 0.04	0.0	-1.0	-0.7 \pm 0.3	1.1	
B2SPC2	18.2	20.1 \pm 1.8	1.0	1.4	1.4 \pm 0.3	0.3				1.0	1.0 \pm 0.1	0.0	-1.0	-1.2 \pm 0.5	0.3	
B1SPC1a	14.9	15.9 \pm 0.7	1.5	1.4	1.4 \pm 0.2	0.0				1.0	1.0 \pm 0.03	0.7	-1.0	-1.1 \pm 0.3	0.2	
B1SPC2	14.9	14.3 \pm 1.9	0.3	1.4	1.7 \pm 0.4	0.9				1.0	1.0 \pm 0.1	0.2	-1.0	-1.4 \pm 0.6	0.7	
P0	18.2	18.1 \pm 1.3	0.1	1.4	1.6 \pm 0.2	1.4				1.0	1.0 \pm 0.1	0.2	-1.0	-1.3 \pm 0.3	1.3	
P1	18.2	18.7 \pm 1.0	0.5	1.4	1.5 \pm 0.2	1.2				1.0	1.0 \pm 0.04	0.0	-1.0	-1.2 \pm 0.2	1.0	
NPCb	1.1	0.8 \pm 0.2	1.3	0.14	0.23 \pm 0.05	1.8				0.9	1.1 \pm 0.1	1.1	-1.0	-1.8 \pm 0.6	1.3	≈ 0.7
B2SPC1b	1.7	0.7 \pm 0.6	1.7	0.11	0.13 \pm 0.05	0.4				1.0	0.4 \pm 0.4	1.5	-1.0	-1.0 \pm 0.8	0.04	
B1SPC1b	1.4	1.4 \pm 0.2	0.2	0.11	0.11 \pm 0.04	0.0				1.0	0.9 \pm 0.1	0.9	-1.0	-1.0 \pm 0.8	0.05	

(a)



(b)

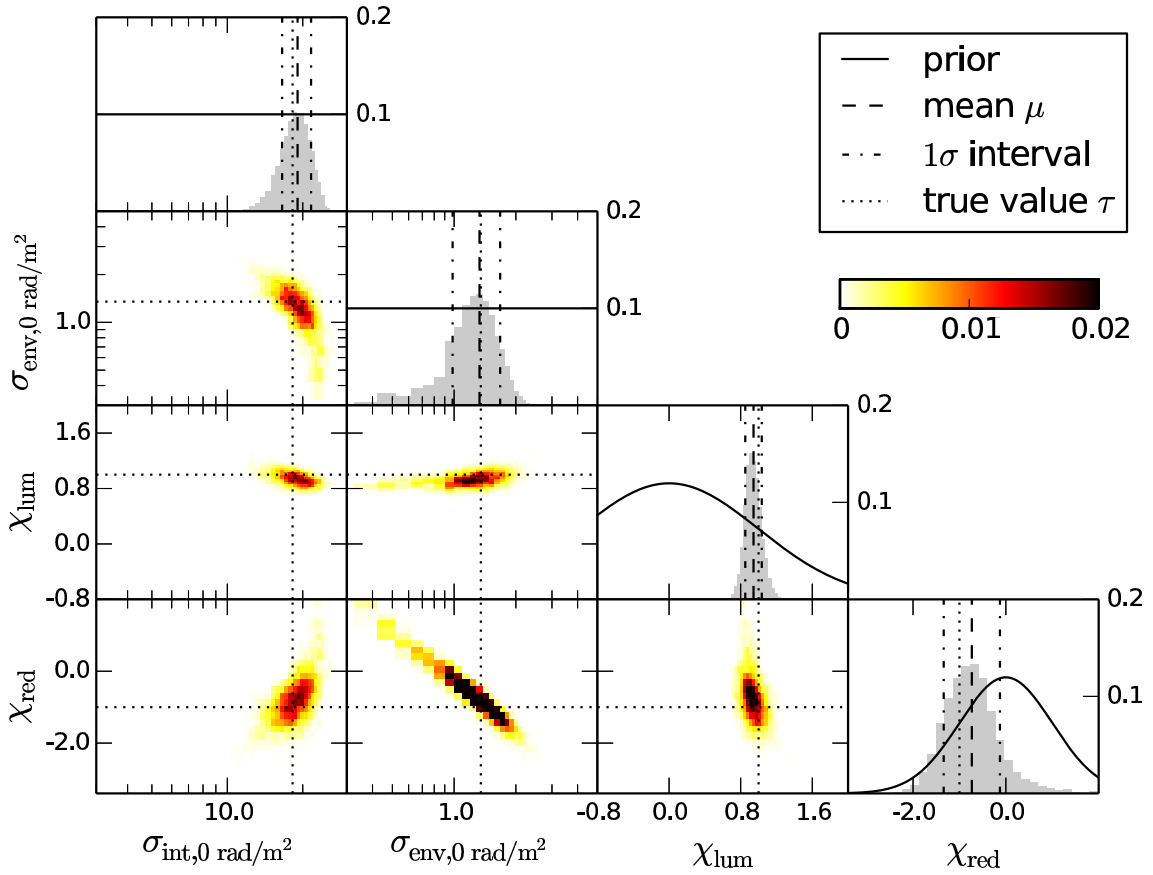
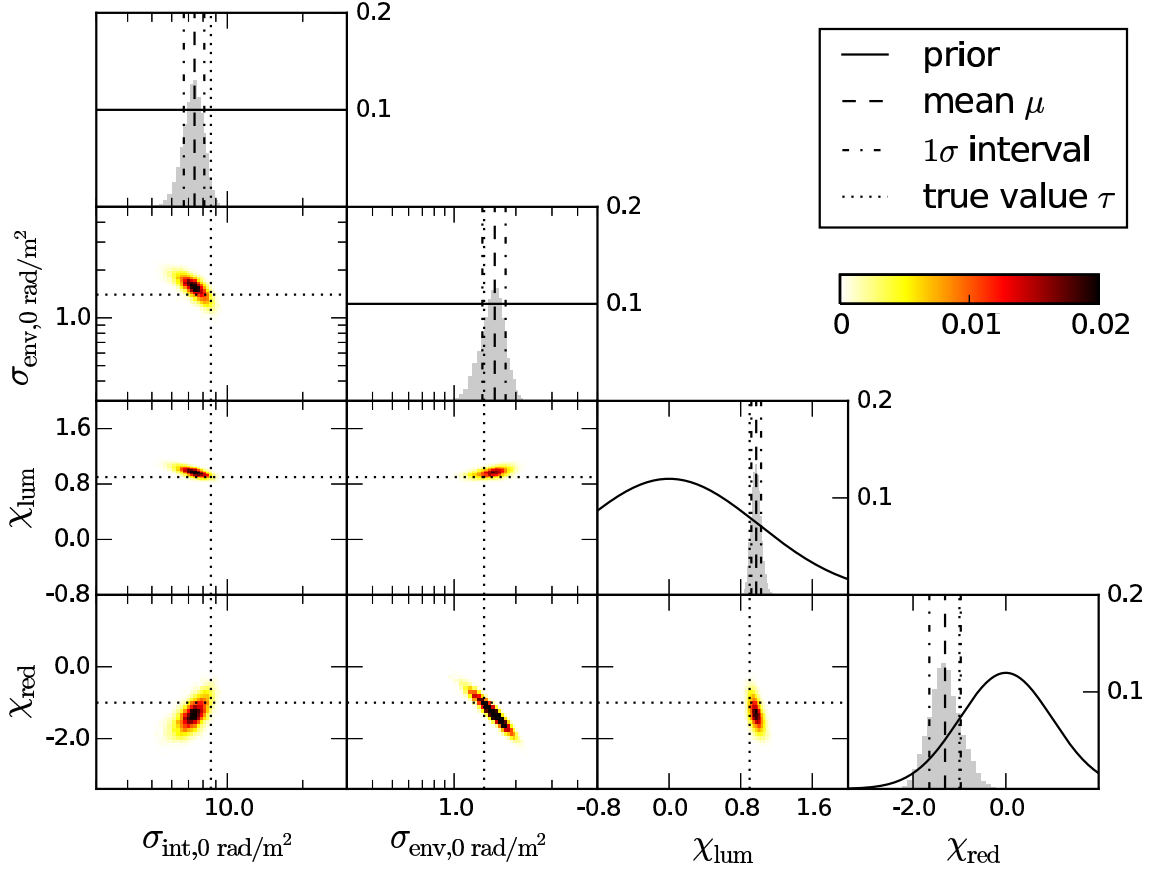


Fig. 2. Results obtained with a two-component scenario for 41632 (2C1) lines of sight in panel (a) and for 4003 (2C2) in panel (b). In each panel the top plots of each column show the 1-dimensional projection of the posterior as well as the true value (dotted line), the outcome of the analysis (dashed and dashed-dotted lines), the prior (continuous line). The panels in color show the 2-dimensional marginalized views of the posterior as

(a)



(b)

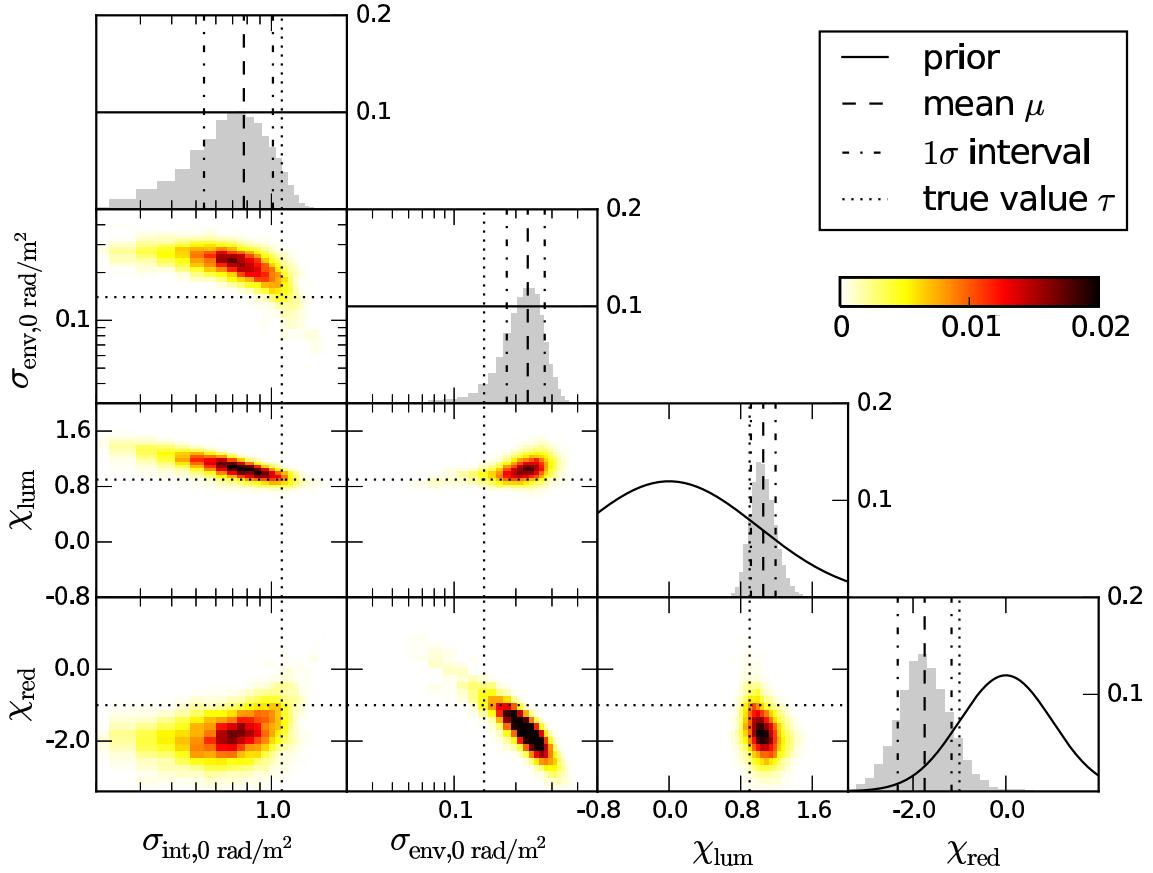
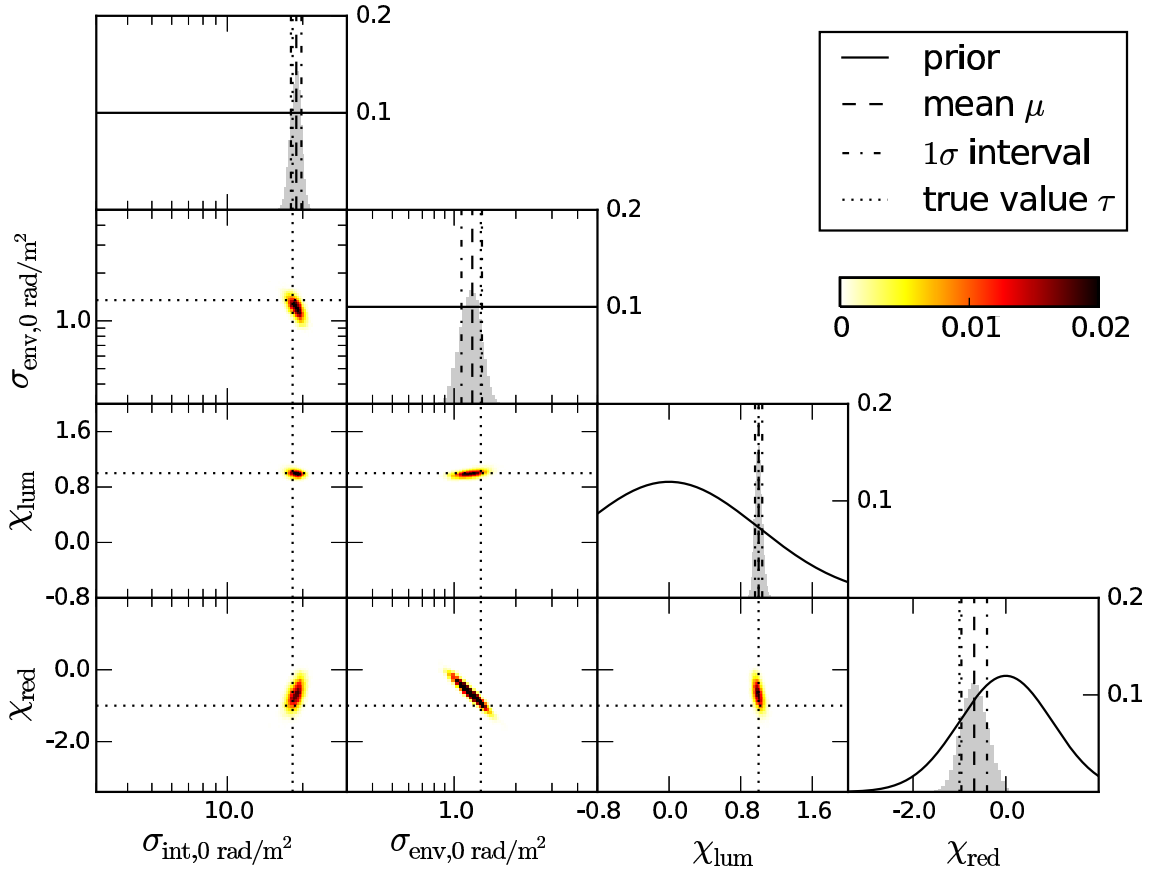


Fig. 3. As Fig. 2 but for results obtained with a two-component scenario for LOFAR HBA observations for $N_{\text{los}} \approx 2200$ and an overall extragalactic standard deviation in Faraday depth of (a) $\approx 7 \text{ rad m}^{-2}$ (NPCa) and (b) $\approx 0.7 \text{ rad m}^{-2}$ (NPCb).

(a)



(b)

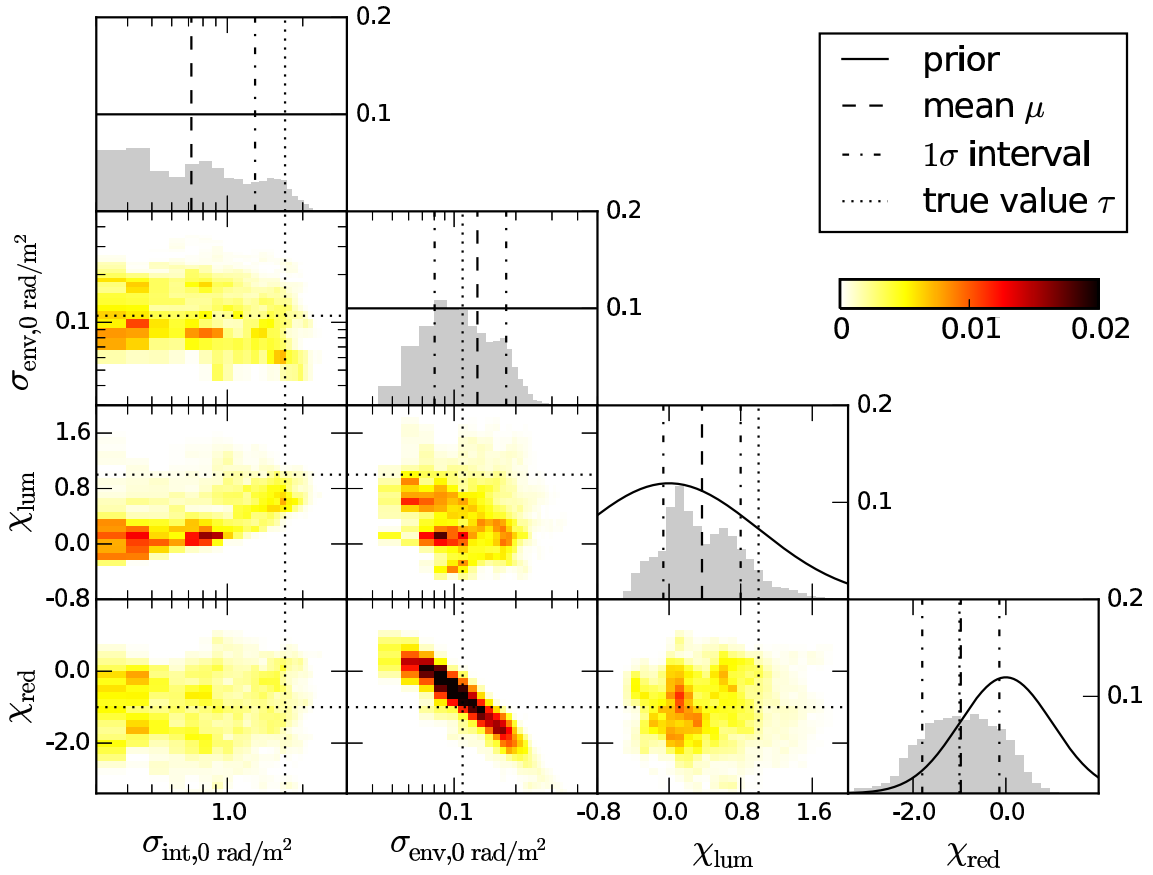


Fig. 4. As Fig. 2 but for results obtained with a two-component scenario for SKA observations in the frequency range 650-1670 MHz for $N_{\text{los}} \approx 3500$ and an overall extragalactic Faraday rotation of (a) $\approx 7.0 \text{ rad m}^{-2}$ (B2SPC1a) and (b) $\approx 0.7 \text{ rad m}^{-2}$ (B2SPC1b).

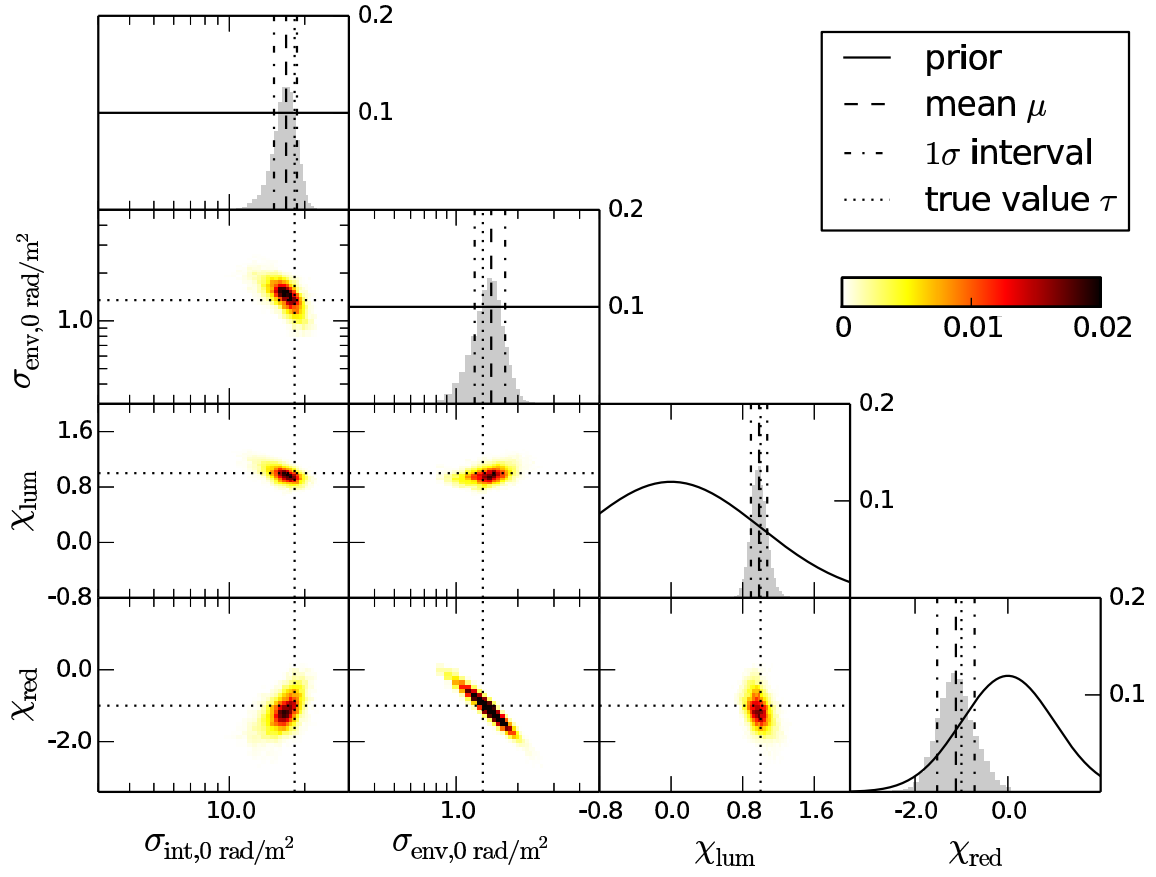


Fig. 5. As Fig. 2 but for results obtained with a two-component scenario for ASKAP observations in the frequency range 1130-1430 MHz for $N_{\text{los}} \approx 3500$ and an overall Faraday depth of $\approx 7.0 \text{ rad m}^{-2}$ (POSSUM).

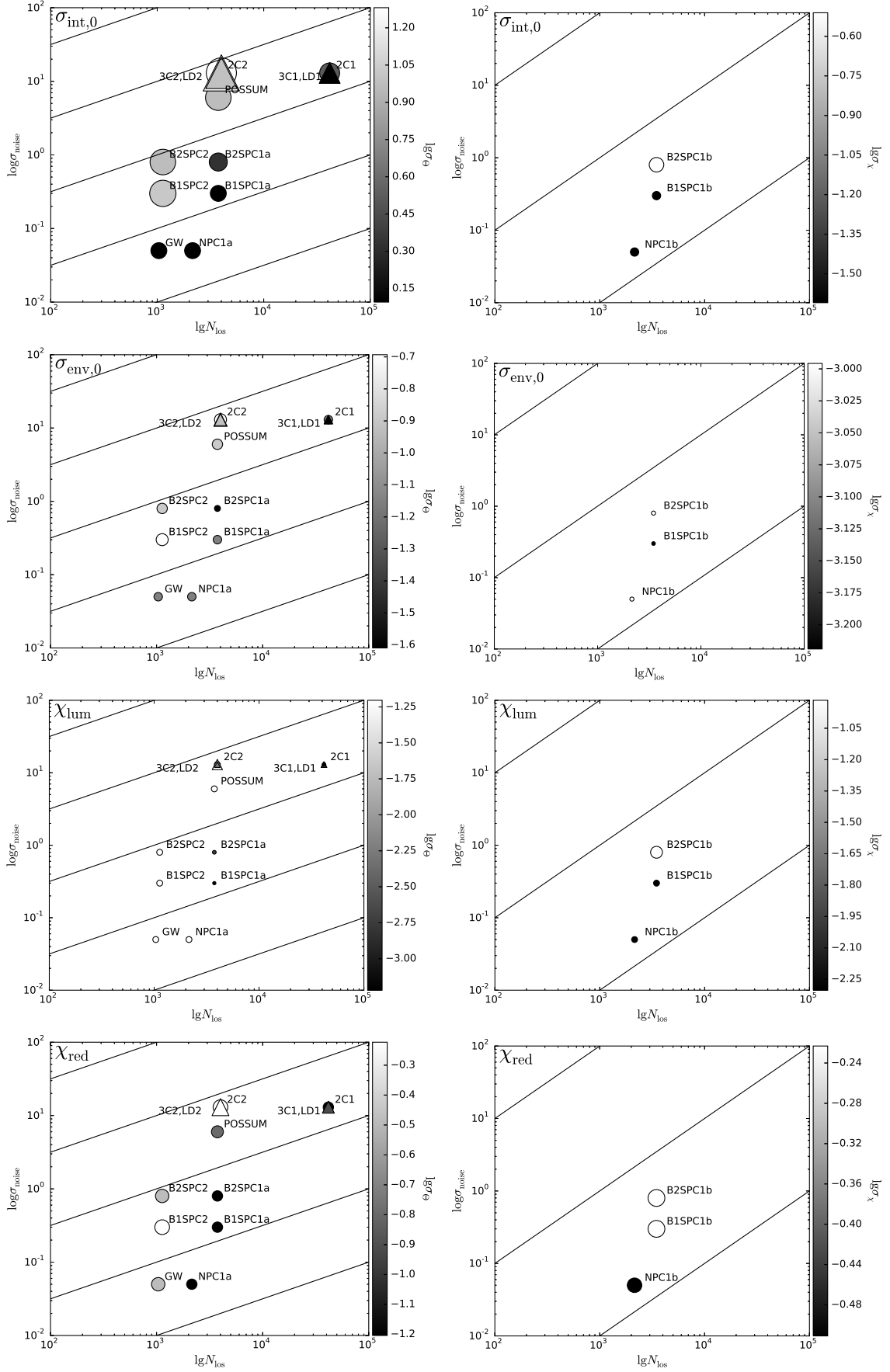


Fig. 6. Uncertainty on $\sigma_{\text{int},0}$, $\sigma_{\text{env},0}$, χ_{lum} , and χ_{red} (from the top to the bottom) as a function of the observational uncertainty σ_{noise} and the number of lines of sight N_{los} for an overall extragalactic Faraday depth variance of $\approx 7.0 \text{ rad m}^{-2}$ (left panels) and $\approx 0.7 \text{ rad m}^{-2}$ (right panels). The size of the points is proportional to the uncertainty on the parameter. A description of this uncertainty is given also by the greyscale. Circles refer to scenarios including two components, while triangles refer to three-component scenarios. Continuous lines correspond to $\sigma_{\text{noise}}^2/N_{\text{los}} = \text{const.}$

Appendix A: Extragalactic Faraday depth variance

In this appendix we derive Eq. (9) from Eq. (5). In Eq. (9) we define the extragalactic Faraday depth variance as

$$\langle \phi_{e,i}^2 \rangle \approx a_0^2 \int_0^{z_i} \frac{dl}{dz} \int_0^{z_i} \frac{dl'}{dz'} \langle n_e(z) n_e(z') B_l(z) B_{l'}(z') \rangle dz dz'. \quad (\text{A.1})$$

This definition can be expressed also as a function of distance along the line of sight l

$$\langle \phi_{e,i}^2 \rangle \approx a_0^2 \int_0^{l(z_i)} dl \int_0^{l(z_i)} dl' \langle n_e(l) n_e(l') B_l(l) B_{l'}(l') \rangle. \quad (\text{A.2})$$

If we assume that the thermal gas density is not characterized by significant fluctuations and define a new variable $r = l' - l$, we have

$$\langle n_e(l) n_e(l') B_l(l) B_{l'}(l') \rangle \approx \langle n_e^2(l) \rangle \langle B_l(l) B_{l'}(l+r) \rangle_{(B_r|n_e)} = \langle n_e^2(l) \rangle C_B(r|n_e), \quad (\text{A.3})$$

where $C_B(r|n_e)$ is the conditional magnetic field correlation function for an environment with thermal gas density n_e . Indeed, we expect the magnetic field strength to be a function of the thermal gas density. With these new definitions, the extragalactic Faraday depth variance reads

$$\langle \phi_{e,i}^2 \rangle \approx a_0^2 \int_0^{l(z_i)} dl \int_{-l}^{l(z_i)-l} dr \langle n_e^2(l) \rangle C_B(r|n_e), \quad (\text{A.4})$$

which can be further simplified if we consider the limit of a infinitely far away source,

$$\langle \phi_{e,i}^2 \rangle \approx a_0^2 \int_0^{z_i} \frac{dl}{dz} dz \langle n_e^2(l(z)) \rangle \int_{-\infty}^{\infty} dr C_B(r|n_e). \quad (\text{A.5})$$

Recalling the definition of correlation length,

$$\Lambda_l = \int dr \frac{C_B(r|n_e)}{\langle B_l^2 \rangle} = \int dl' \frac{\langle B(l) B(l') \rangle}{\langle B(l)^2 \rangle}, \quad (\text{A.6})$$

we obtain

$$\langle \phi_{e,i}^2 \rangle = a_0^2 \int_0^{z_i} \frac{dl}{dz} dz \langle n_e^2(l(z)) \rangle \Lambda_l(n_e) \langle B^2 \rangle_{(B|n_e)}. \quad (\text{A.7})$$

As described in Sec. 2, in a homogeneous Universe $n_e = n_{e0}(1+z)^3$, $\Lambda_l = \Lambda_{l0}(1+z)^{-1}$, and $\langle B^2 \rangle = \langle B_0^2 \rangle(1+z)^4$. Therefore,

$$\langle \phi_{e,i}^2 \rangle = a_0^2 \int_0^{z_i} \langle n_0^2 \rangle \Lambda_{0l} \langle B_{0l}^2 \rangle \frac{dl}{dz} (1+z)^5 dz, \quad (\text{A.8})$$

where the increment in wavelength due to the expansion of the Universe has been taken into account as well and we have assumed $z(l) \approx z(l+r)$. If we use the definition of proper displacement along a light-ray $dl/dz = c(1+z)^{-1}/H(z)$, this finally leads to Eq. (9),

$$\langle \phi_{e,i}^2 \rangle = a_0^2 \int_0^{z_i} \langle n_0^2 \rangle \Lambda_{0l} \langle B_{0l}^2 \rangle \frac{c}{H(z)} (1+z)^4 dz. \quad (\text{A.9})$$

In an inhomogeneous Universe with different environments, the differential variance in each environment is

$$\frac{d\sigma_{RM}^2(n_e)}{dx} = \langle n_e^2(z) \rangle \langle B^2 \rangle_{(B|n_e)}. \quad (\text{A.10})$$

Therefore, it follows

$$\langle \phi_{e,i}^2 \rangle = a_0^2 \int_0^{z_i} \frac{dx}{dz} \frac{dz}{(1+z)^4} \int dn_e P(n_e|z) \frac{d\sigma_{RM}^2(n_e)}{dx}, \quad (\text{A.11})$$

where the integral can be replaced by a discrete sum over typical environments (see also Eq. (30)).

Appendix B: Convergence

We start the algorithm from two random positions in the Θ -space and then explore the space⁶ until convergence. Each of these two sequences of steps in the Θ -space is called Gibbs chain. To assess convergence of each Gibbs chain, we require the following conditions to be satisfied:

- the number of steps taken from each chain to be at least about $10l_c$ for each parameter, where l_c is the number of steps at which the correlation coefficient drops to 10%;
- the Gelman and Rubin test (Gelman & Rubin 1992; Brooks & Gelman 1997). We evaluate the intra-chain variance

$$I = \frac{1}{m} \sum_{j=1}^m s_j^2 \quad (\text{B.1})$$

and the inter-chain variance

$$B = \frac{n}{m-1} \sum_{j=1}^m (\theta_j - \theta)^2 \quad (\text{B.2})$$

for our Θ parameters and use them to compute the potential scale reduction factor R defined as

$$R = \sqrt{1 - \frac{1}{n} + \frac{B}{nI}}, \quad (\text{B.3})$$

where m is the number of chains, n is the half-length of each chain, θ_j and s_j are respectively the mean and the standard deviation of the j th chain, while θ_j is the mean of the chain j and θ is the variance of the chain means. We require $R = 1$ within a few percents for each parameter.

We consider the chains to be converged when both these conditions are satisfied.

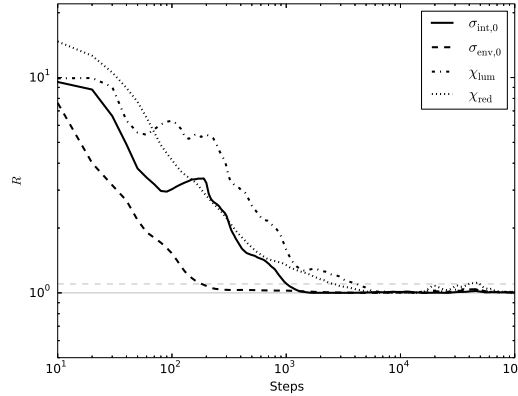


Fig. B.1. Potential scale reduction factor R evaluated every 10 samples for the parameters $\sigma_{\text{int},0}$, $\sigma_{\text{env},0}$, χ_{lum} , and χ_{red} , as a function of the number of steps in the MCMC. The continuous and the dashed lines represent a potential scale reduction factor equal to 1.0 and 1.1, respectively. It can be seen that the Gelman and Rubin test indicates convergence after typically a few thousand steps.

As an example, in Fig. B.1 we show the plot of the potential scale reduction factor R versus the number of steps for the Θ parameters in the scenario 2C1. The potential scale reduction factor has been evaluated every 10 samples. After about 5000 steps we obtain $R = 1$ within a few percent. In Table B.1 the potential scale reduction factor R for each parameter of each test is reported. For present-instrument (scenario 2C1), LOFAR (scenario NPCa) and SKA (scenario B2SPC1a) observations, in Fig. B.2 we show the correlation coefficient ρ_j

$$\rho_j(k) = \frac{\sum_{s=1}^{2n-k} (x_s - \theta_j)(x_{s+k} - \theta_j)}{\sum_{s=1}^{2n} (x_s - \theta_j)^2}, \quad (\text{B.4})$$

as a function of the number of steps for each parameter $\sigma_{\text{int},0}$, $\sigma_{\text{env},0}$, χ_{lum} , and χ_{red} . Here x_s is the value of one of these parameters for a given step. For all the parameters in the scenario 2C1, l_c turns out to be ≈ 3000 , while for the scenarios NPCa and B2SPC1a, the correlation length is about 500-1000. In these plots the steps in the burn-in phase have been discarded by visual inspection.

⁶ We tuned the variance of the Gaussian step proposal to ensure an acceptance rate of the Metropolis-Hastings algorithm of approximately 15-30%

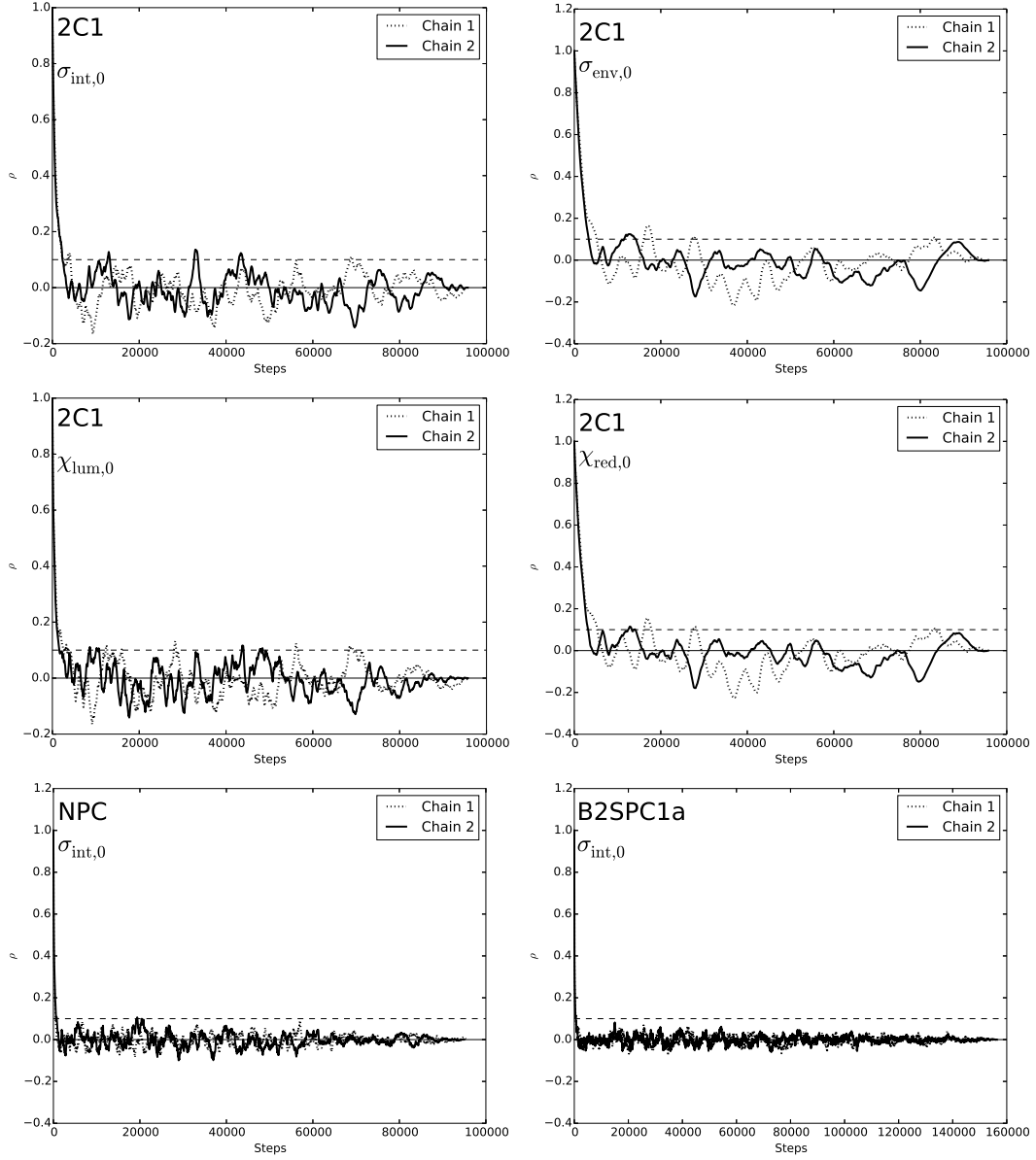


Fig. B.2. Correlation coefficient ρ as a function of the number of steps in the MCMC for the four Θ parameters in the 2C1 test (top and middle panels) and for the $\sigma_{\text{int},0}$ parameter in the LOFAR NPC and the SKA B2SPC1a tests (bottom panels). The steps in the burn-in phase have been discarded. The dashed line indicates a correlation coefficient of 0.1, while the continuous line the zero-level.

Appendix C: Alternative scenarios

In this appendix we present the application to scenarios including three components, representing:

- an intrinsic, an environmental, and a constant contribution (scenario 3C),

$$\sigma_{e,i}^2(z_i, \Theta) = \left(\frac{L}{L_0} \right)^{\chi_{\text{lum}}} \frac{\sigma_{\text{int},0}^2}{(1+z_i)^4} + \frac{D_i(z_i, \chi_{\text{red}})}{D_0} \sigma_{\text{env},0}^2 + \sigma_c^2 \quad (\text{C.1})$$

The constant contribution σ_c^2 takes into account terms that are not described by the parameterization of the other two but that could nevertheless be present in our data (e.g. the ionosphere, under the assumption that this does not show any direction-dependence);

- an intrinsic, an environmental, and a latitude-dependent contribution (scenario LD),

$$\sigma_{e,i}^2(z_i, \Theta) = \left(\frac{L}{L_0} \right)^{\chi_{\text{lum}}} \frac{\sigma_{\text{int},0}^2}{(1+z_i)^4} + \frac{D_i(z_i, \chi_{\text{red}})}{D_0} \sigma_{\text{env},0}^2 + p(b) \sigma_{\text{lat}}^2 \quad (\text{C.2})$$

where $p(b)$ is the Galactic profile from Oppermann et al. (2015). The latitude-dependent contribution $p(b) \sigma_{\text{lat}}^2$ may explain a residual latitude dependence not taken into account in the modeling of Oppermann et al. (2015), e.g. an uncorrelated Galactic signal not captured by their analysis.

Table B.1. Potential scale reduction factor R from the Gelman and Rubin test.

ID	$\sigma_{\text{int},0}$	$\sigma_{\text{env},0}$	$\chi_{\text{c/lat}}$	χ_{lum}	χ_{red}
2C1	1.00	1.01		1.00	1.01
2C2	1.00	1.01		1.00	1.01
3C1	1.01	1.12	1.07	1.00	1.09
3C2	1.00	1.00	1.00	1.01	1.00
LD1	1.03	1.05	1.00	1.02	1.04
LD2	1.00	1.01	1.01	1.00	1.01
GW	1.00	1.00		1.00	1.00
NPCa	1.00	1.00		1.00	1.00
POSSUM	1.02	1.03		1.01	1.03
B2SPC1a	1.00	1.01		1.00	1.01
B2SPC2	1.00	1.00		1.00	1.00
B1SPC1a	1.00	1.00		1.00	1.00
B1SPC2	1.00	1.00		1.00	1.00
P0	1.02	1.03		1.01	1.03
P1	1.01	1.02		1.00	1.02
NPCb	1.00	1.00		1.00	1.00
B2SPC1b	1.45	1.08		1.01	1.03
B1SPC1b	1.04	1.02		1.01	1.01

As for the simplest 2C-scenario, for each of these scenarios we run two tests corresponding to 41632 and 4003 lines of sight. Fig. C.1 and Fig. C.2 show the results respectively when a third constant component (tests 3C1 and 3C2) and latitude-dependent component (tests LD1 and LD2) are included. In both figures, we show the plots for 41632 lines of sight in panel (a) and for 4003 lines of sight in panel (b).

These plots indicate that the algorithm performs well also when three components are considered. As expected, the values of the Θ parameters recovered are less accurate when a lower number of lines of sight is used. The additional parameters tend to lead to a slight increase in the posterior uncertainty for the other parameters when comparing with the results of 2C1 and 2C2.

Appendix D: Priors

In order to get a data-driven solution and to keep our assumptions as general as possible, an uninformative prior should be adopted for the Θ parameters. Since we included in our model all the main redshift and luminosity dependencies, the Gaussian prior in Eq. (21) is suitable for χ_{lum} and χ_{red} . Concerning $\sigma_{\text{int},0}$ and $\sigma_{\text{env},0}$, we may ask if different priors can have an impact on our results. In Sect. 3.1, we adopted a flat-prior,

$$P(\sigma) = \text{const.} \quad (\text{D.1})$$

In this appendix we present two tests corresponding to extreme choices of these priors. Indeed, we considered a flat prior in σ^2 (scenario P1)

$$P(\sigma^2) = \text{const.}, \quad (\text{D.2})$$

and a flat prior in $\ln(\sigma^2)$ (scenario P0)

$$P(\ln(\sigma^2)) = \text{const.} \quad (\text{D.3})$$

In Fig. D.1 we show the results for the two priors: flat in σ^2 in panel (a) and flat in $\ln(\sigma^2)$ in panel (b).

The first choice is an optimistic prior, since it implies a suppression of σ values $\ll 1$, pushing for the recovery of larger, possibly ~ 1 values of σ . The second choice is a pessimistic prior since it would weight all small and large σ values in the same way, favoring negligible extragalactic contributions, easily compatible with the data due to the shape of the likelihood. We stress that the final results are not affected by the choice of the prior. However, this choice has an impact on the convergence-time, since the starting point of each chain is randomly extracted from the prior. For example, for a flat prior in $\ln(\sigma^2)$, the chances to extract a very small σ value ($\ll 1$) are larger than for the prior used in Sect. 3.1, possibly making the convergence time very long. For these tests, the number of lines of sights and the assumed noise properties are the same as in the 2C1 test.

Appendix E: LOFAR

An interesting region of the sky is represented by the Great Wall, where one of the largest filaments of optical galaxies has been observed (Gott et al. 2005). We generate a mock collection of source coordinates in a region of the sky as large as this region ($7.5^{\text{h}} < \text{RA} < 17.5^{\text{h}}$ and $25^{\circ} < \text{Dec} < 65^{\circ}$), considering a density of one polarized sources per 1.7 square degrees (survey of 8 h per pointing) and Galactic latitude $b > 55^{\circ}$. This results in $N_{\text{los}} \approx 1000$ and a maximum uncertainty in Faraday depth $\sigma_{\text{noise}} = 0.05 \text{ rad m}^{-2}$. We will refer to this mock catalog in the following as GW. The results for an overall extragalactic Faraday rotation of $\approx 7.0 \text{ rad m}^{-2}$ are shown in Fig. E.1 and indicate that it is possible to disentangle the intrinsic and environmental contributions already with a number of lines of sight of about one thousand.

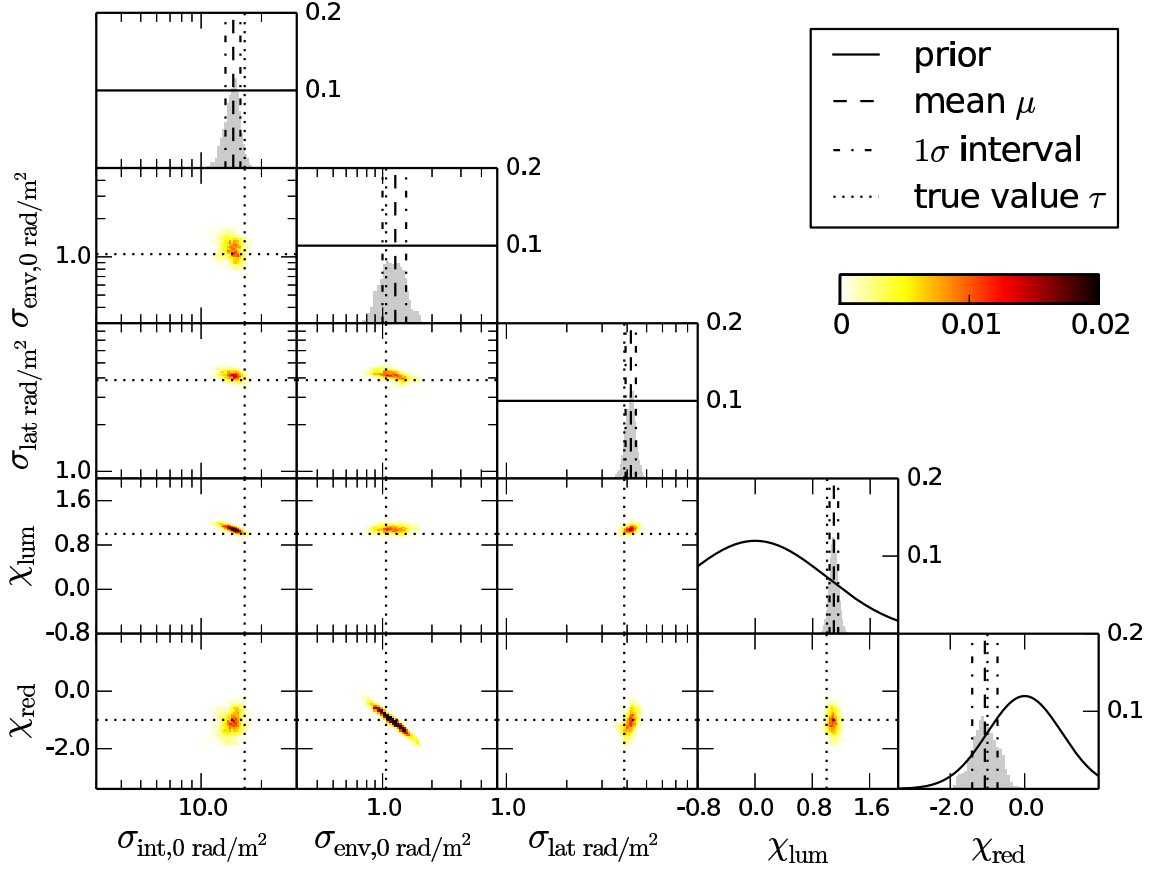
Appendix F: SKA

In this appendix we investigate the performance in the frequency band 1 (B1), meaning 350-1050 MHz, with the same collection of sources (approximately 3500) described in Sect. 3.2.2. According to Stepanov et al. (2008), this frequency range corresponds to an expected maximum uncertainty in Faraday depth of 0.3 rad m^{-2} , for a $S/N > 5$. We will refer to this catalog as B1SPC1. We generate mock rotation measure catalogs considering an overall extragalactic Faraday rotation of $\approx 7.0 \text{ rad m}^{-2}$ (B1SPC1a) as well as $\sigma_e \approx 0.7 \text{ rad m}^{-2}$ (B1SPC1b). In Fig. F.1 we show the results. These tests indicate that a catalog in band 1 allows derivation of better constraints than a catalog in band 2. This becomes particularly evident for an overall extragalactic Faraday rotation of $\approx 0.7 \text{ rad m}^{-2}$.

Additionally, we examine the case when a smaller number of lines of sight is available. Therefore, we generate a catalog corresponding to a density of one polarized source per three square degrees, including all the sources with Galactic latitude $b < -55^\circ$. This translates in $N_{\text{los}} \approx 1000$. We will refer to these catalogs as B1SPC2 and B2SPC2, respectively for the frequency ranges corresponding to band 1 and band 2. We generate these catalogs assuming an overall extragalactic Faraday rotation of $\approx 7 \text{ rad m}^{-2}$. In Fig. F.2 we show the results for both frequency bands.

When data in the frequency range from 350 to 1670 MHz are used, already a number of lines of sight of the order of one thousand is enough to disentangle the contribution intrinsic to the source from the one due to the environment between the source and the observer for $\sigma_e \approx 7.0 \text{ rad/m}^2$. Our results indicate that the posterior distributions narrow moving to lower frequencies with the best performance obtained in the frequency band 350-1050 MHz. At higher frequencies the posteriors are broader but with mean values still in agreement with the real values.

(a)



(b)

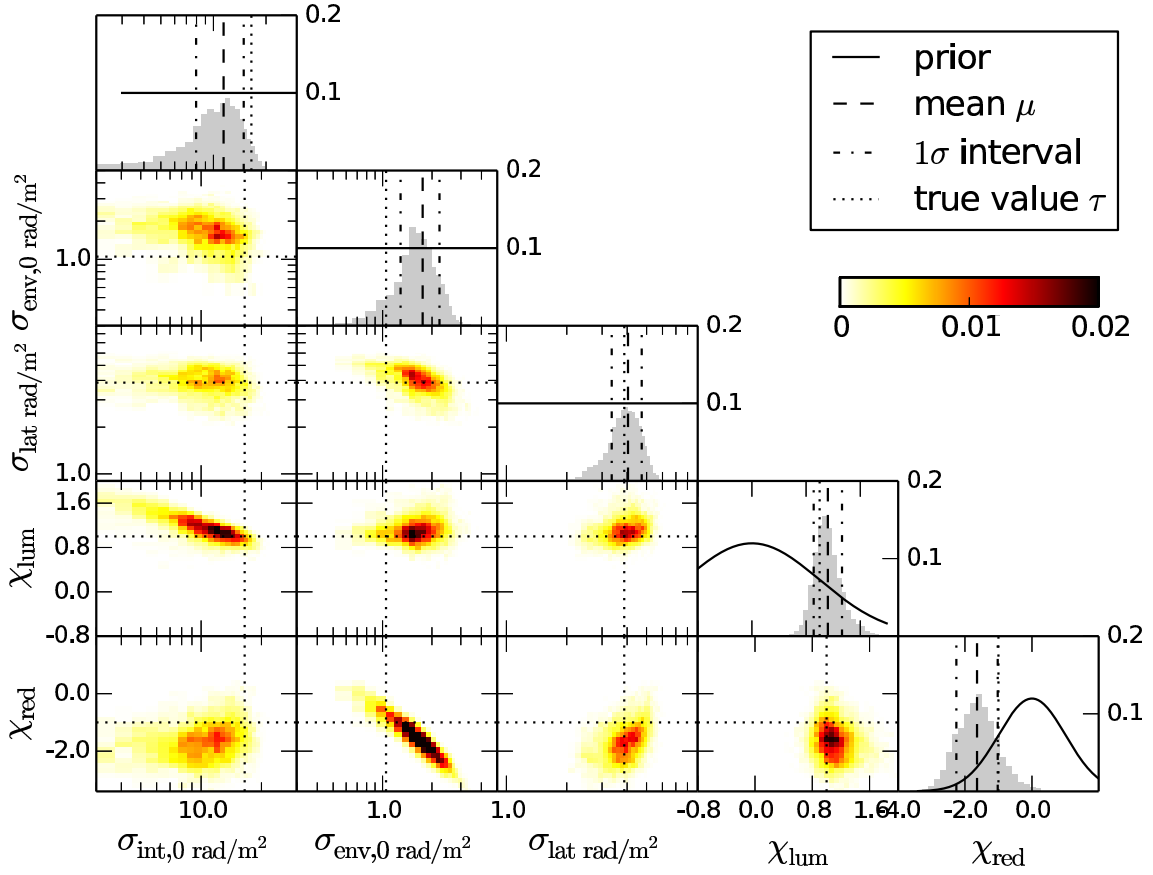
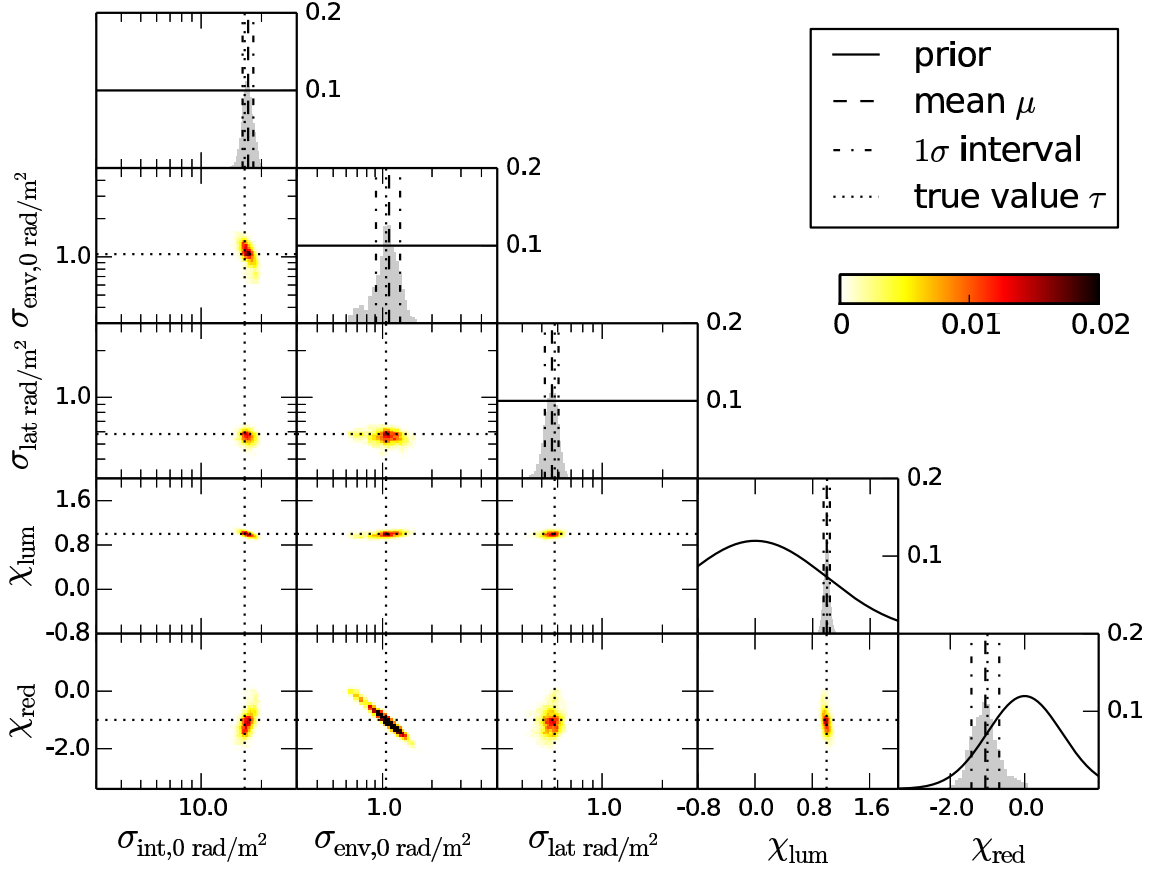


Fig. C.1. Results obtained with a three-component scenario, including a constant contribution, for 41632 (3C1) lines of sight (a) and 4003 (3C2) lines of sight (b).

(a)



(b)

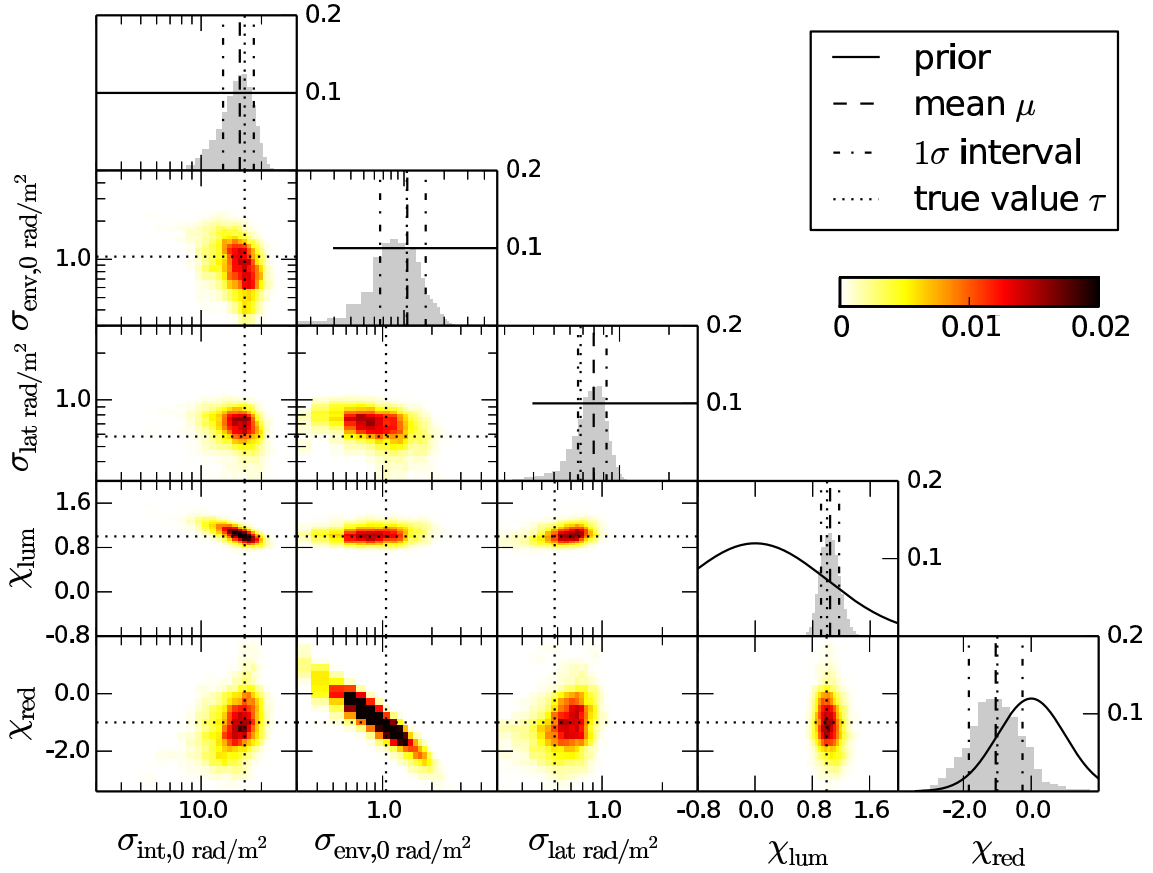
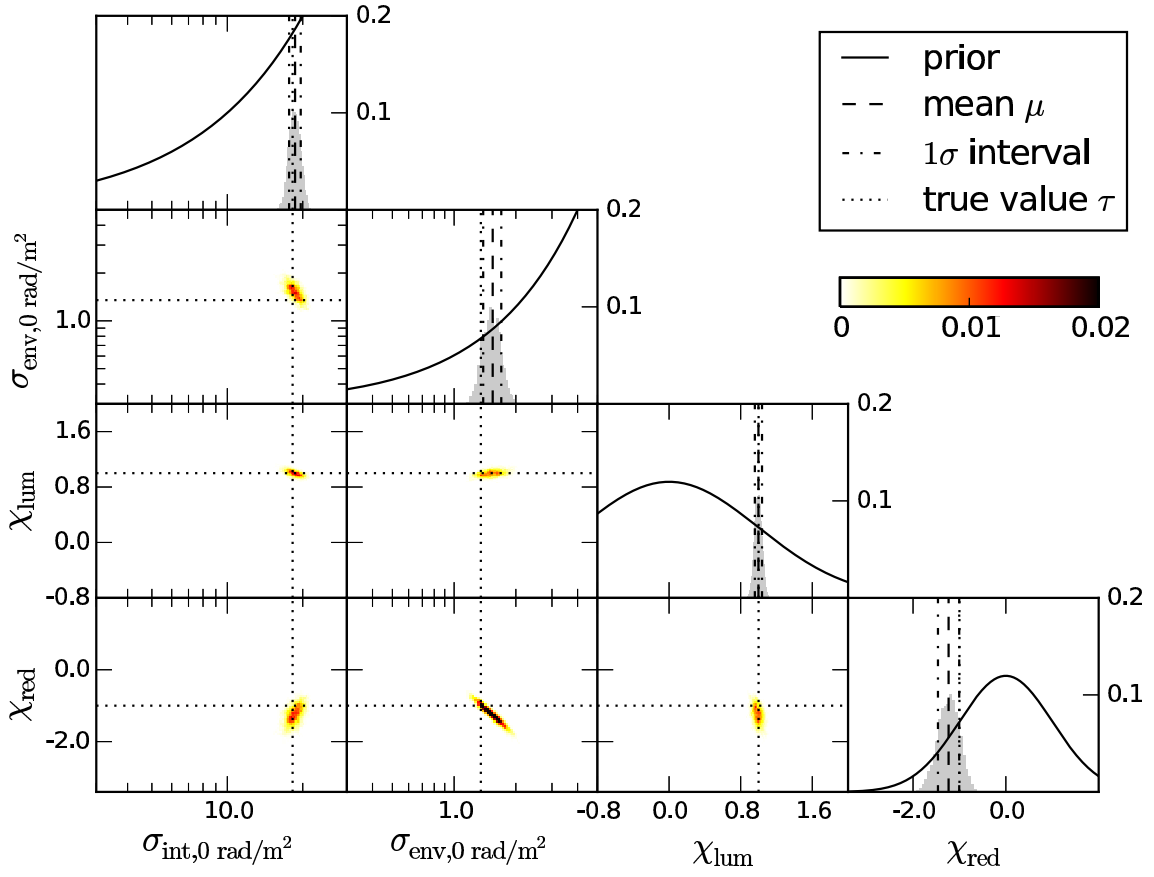


Fig. C.2. Results obtained with a three-component scenario, including a latitude-dependent contribution, for 41632 (LD1) lines of sight (a) and 4003 (LD2) lines of sight (b).

(a)



(b)

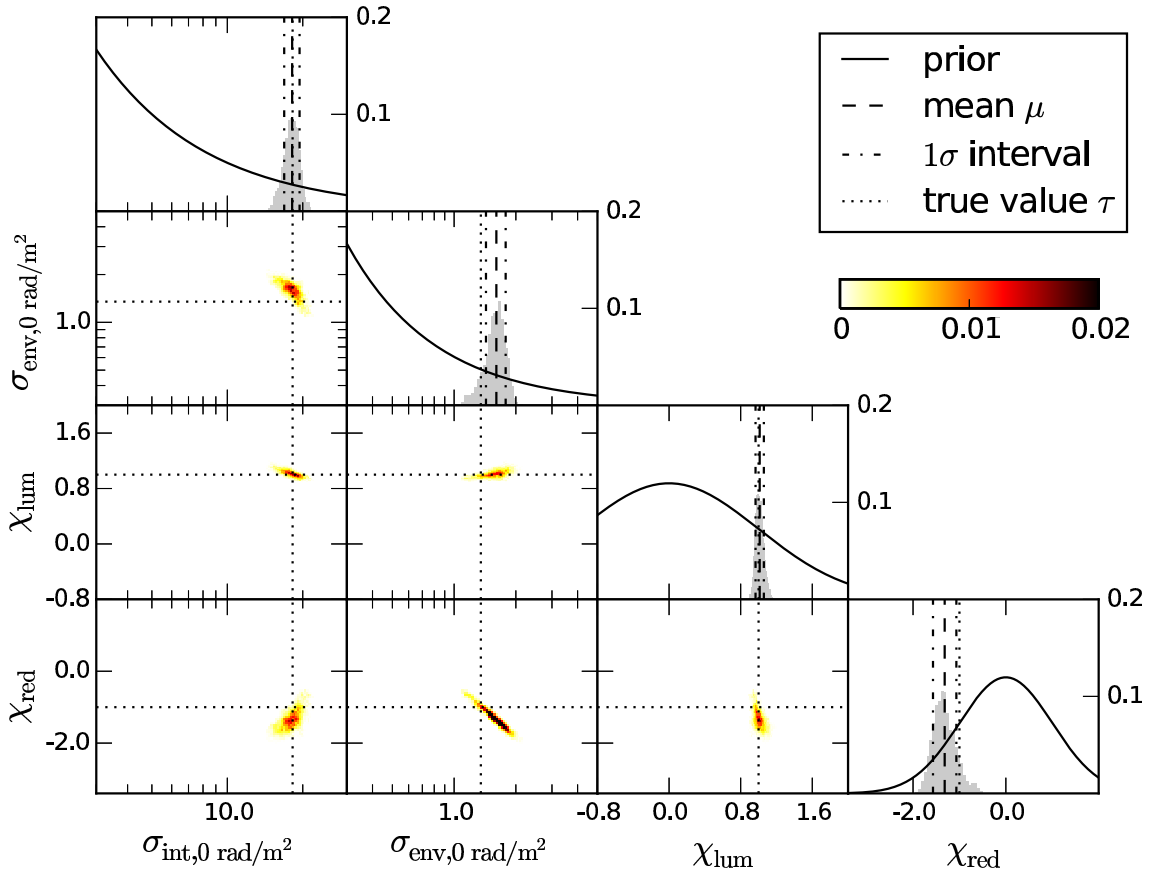


Fig. D.1. Results obtained with a two-component scenario and an overall extragalactic Faraday 7 rad m⁻² for (a) a flat prior in σ^2 (P1) and for (b) a flat prior in $\ln(\sigma^2)$ (P0) for 41632 lines of sight.

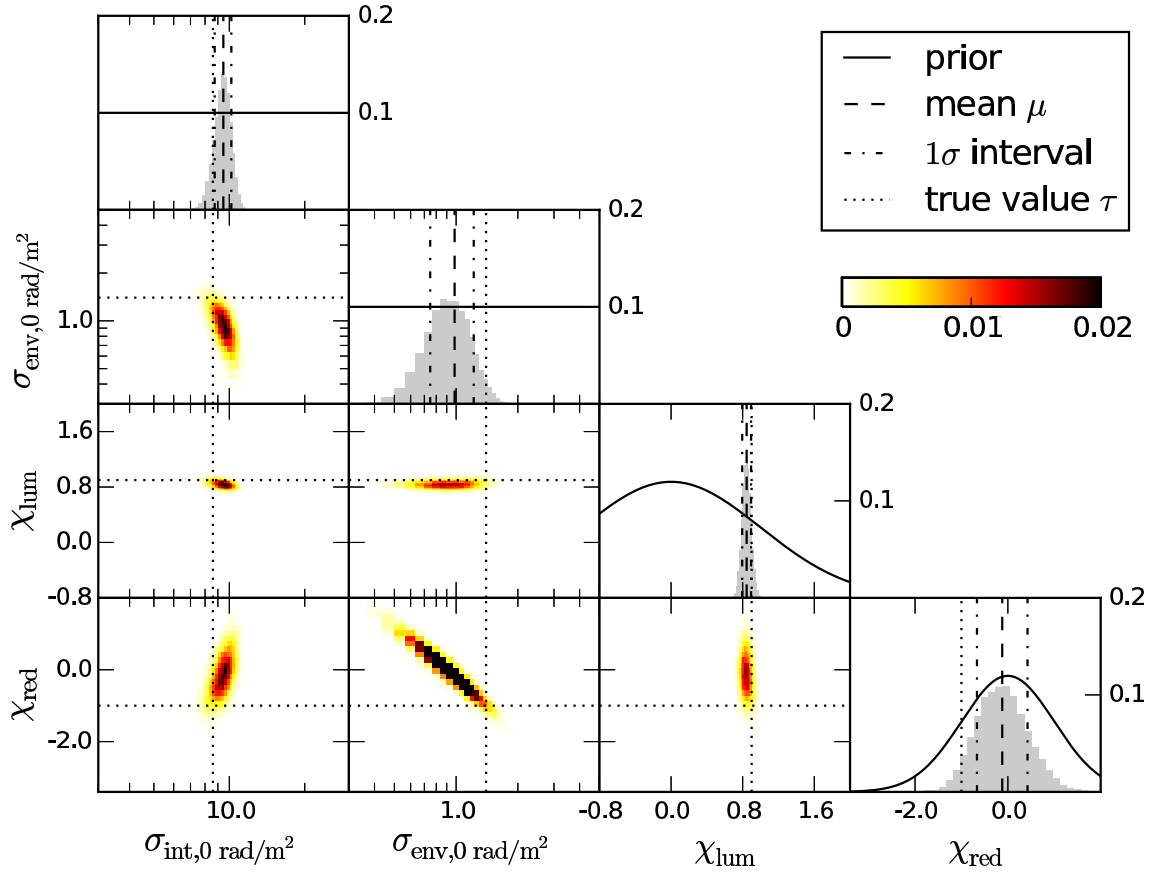
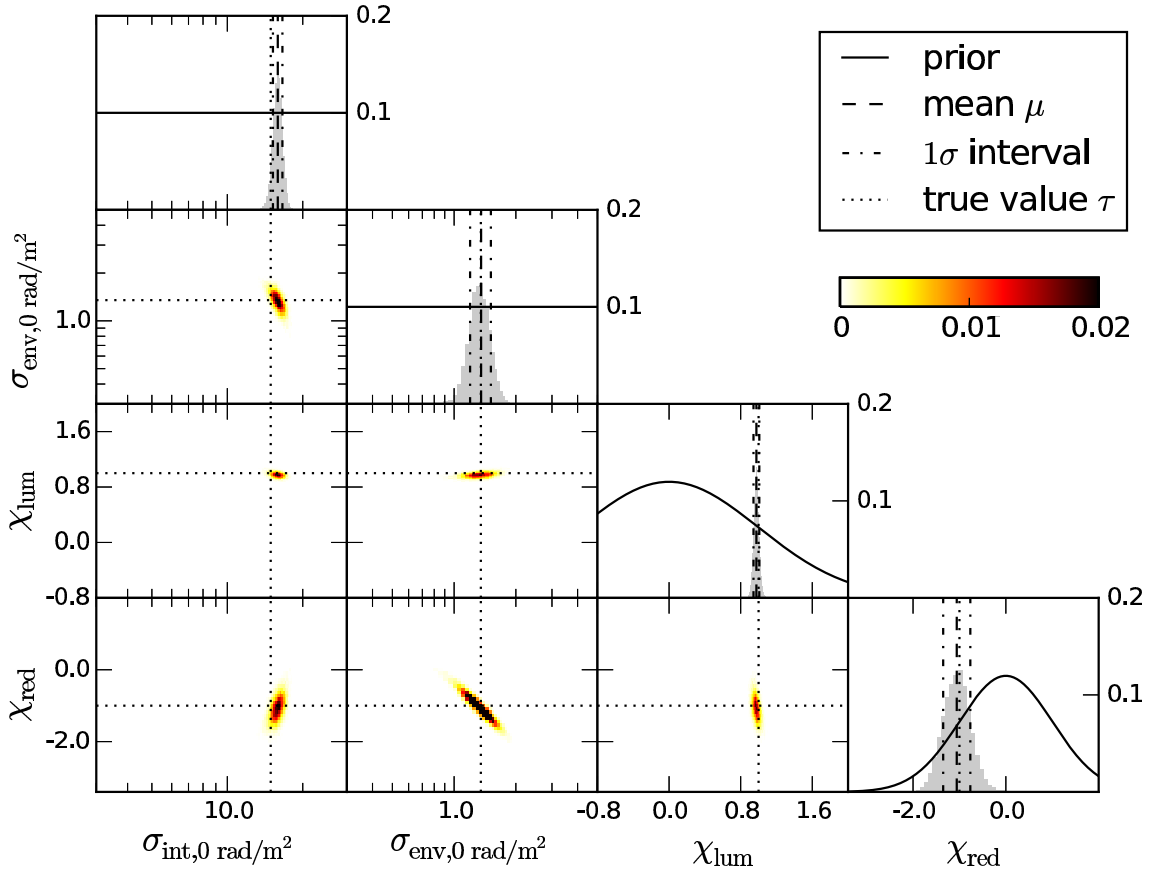


Fig. E.1. Results obtained with a two-component scenario for LOFAR HBA observations for an overall Faraday depth of $\approx 7.0 \text{ rad m}^{-2}$ and $N_{\text{los}} \approx 1000$ (GW).

(a)



(b)

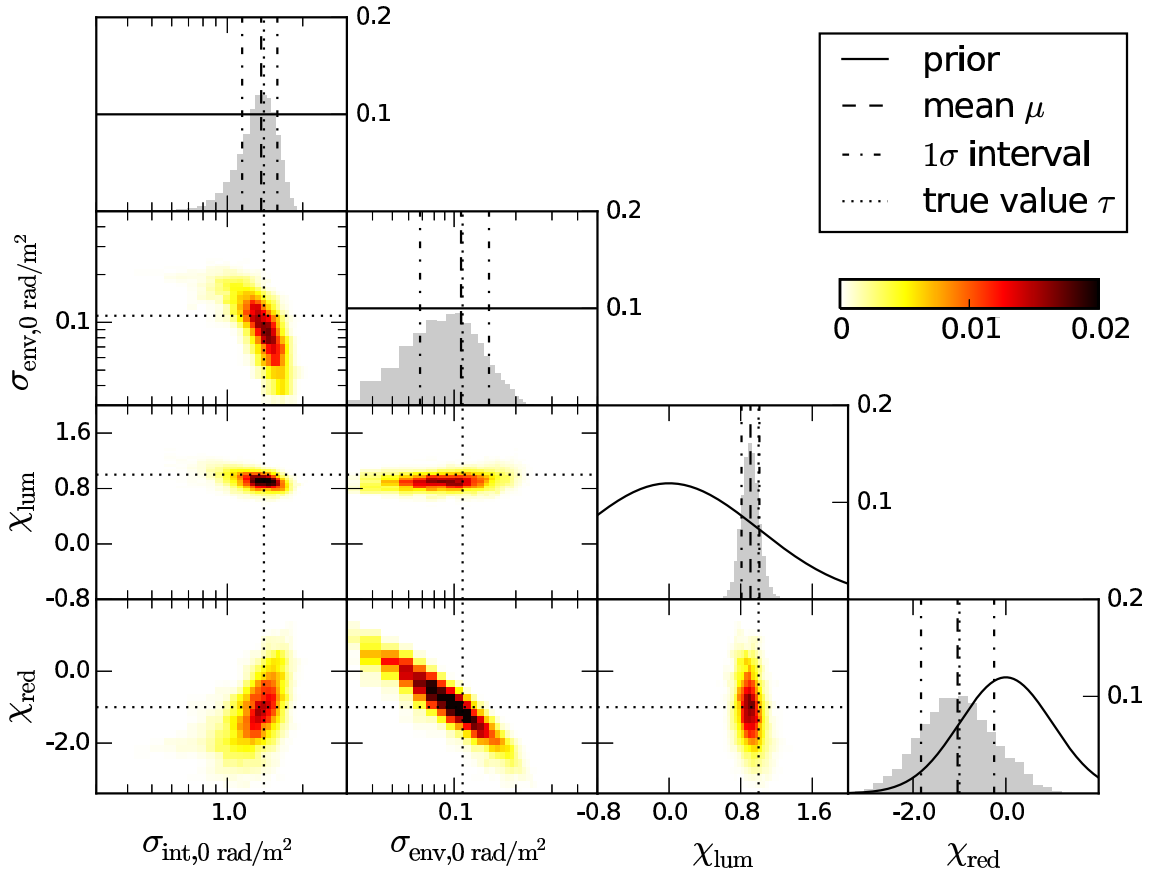


Fig. F.1. Results obtained with a two-component scenario for SKA observations in the frequency range 350-900 MHz for $N_{\text{los}} \approx 3500$ and an overall Faraday depth of (a) $\approx 7.0 \text{ rad m}^{-2}$ (B1SPC1a) and (b) $\approx 0.7 \text{ rad m}^{-2}$ (B1SPC1b).

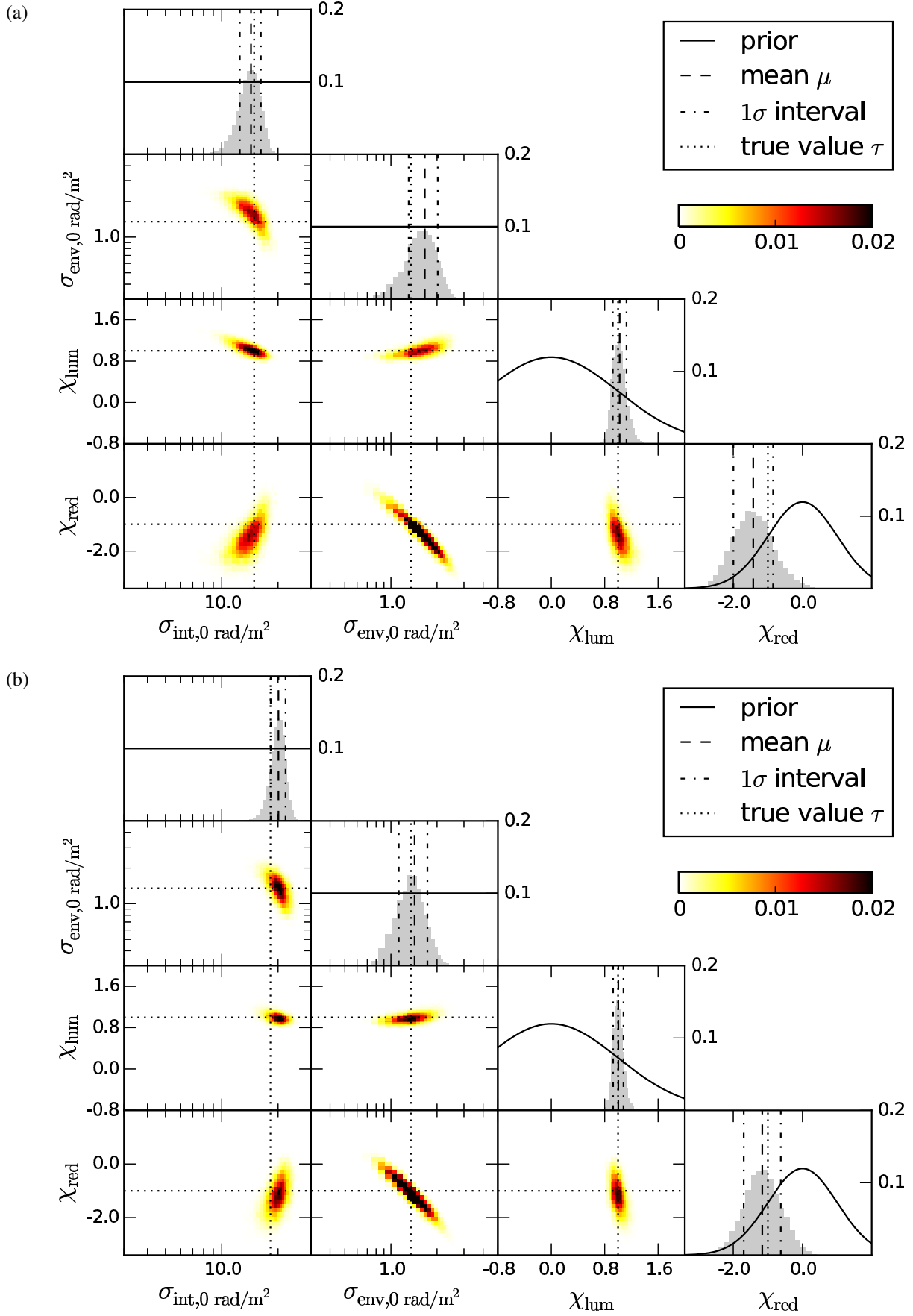


Fig. F.2. Results obtained with a two-component scenario for SKA observations in the frequency range (a) 350-900 MHz (B1SPC2) and (b) 650-1670 MHz (B2SPC2) for $N_{\text{los}} \approx 1000$ and an overall Faraday depth of $\approx 7.0 \text{ rad m}^{-2}$.